

Abyssal Slope Currents

ESTHER CAPÓ,^a JAMES C. MCWILLIAMS,^a JONATHAN GULA,^{a,b} M. JEROEN MOLEMAKER,^a
PIERRE DAMIEN,^a AND RENÉ SCHUBERT^b

^a Department of Atmospheric and Oceanic Sciences, University of California, Los Angeles, Los Angeles, California

^b Univ. Brest, CNRS, IRD, Ifremer, Laboratoire d'Océanographie Physique et Spatiale, IUEM, Brest, France

(Manuscript received 15 February 2024, in final form 22 August 2024, accepted 11 September 2024)

ABSTRACT: Realistic computational simulations in different oceanic basins reveal prevalent prograde mean flows (in the direction of topographic Rossby wave propagation along isobaths; aka topostrophy) on topographic slopes in the deep ocean, consistent with the barotropic theory of eddy-driven mean flows. Attention is focused on the western Mediterranean Sea with strong currents and steep topography. These prograde mean currents induce an opposing bottom drag stress and thus a turbulent boundary layer mean flow in the downhill direction, evidenced by a near-bottom negative mean vertical velocity. The slope-normal profile of diapycnal buoyancy mixing results in downslope mean advection near the bottom (a tendency to locally increase the mean buoyancy) and upslope buoyancy mixing (a tendency to decrease buoyancy) with associated buoyancy fluxes across the mean isopycnal surfaces (diapycnal downwelling). In the upper part of the boundary layer and nearby interior, the diapycnal turbulent buoyancy flux divergence reverses sign (diapycnal upwelling), with upward Eulerian mean buoyancy advection across isopycnal surfaces. These near-slope tendencies abate with further distance from the boundary. An along-isobath mean momentum balance shows an advective acceleration and a bottom-drag retardation of the prograde flow. The eddy buoyancy advection is significant near the slope, and the associated eddy potential energy conversion is negative, consistent with mean vertical shear flow generation for the eddies. This cross-isobath flow structure differs from previous proposals, and a new one-dimensional model is constructed for a topostrophic, stratified, slope bottom boundary layer. The broader issue of the return pathways of the global thermohaline circulation remains open, but the abyssal slope region is likely to play a dominant role.

KEYWORDS: Abyssal circulation; Bottom currents; Diapycnal mixing; Topographic effects; Upwelling/downwelling; Regional models

1. Introduction

The abyssal ocean below the pycnocline is little explored relative to the upper ocean. It is understood to be generally full of mesoscale eddy currents that reach deeply down from the pycnocline, inertia–gravity waves generated at both the bottom and surface, stratified shear turbulence, a turbulent bottom boundary layer with topographic vortical wakes extending into the interior, submesoscale coherent vortices, and narrow deep western boundary currents that are part of the global thermohaline circulation. This paper is about additional phenomena that as yet are even less well understood.

The first of these phenomena is topostrophy (Holloway 2008), defined as a prograde time-mean along-isobath current over a sloping bottom (i.e., in the same direction as the phase propagation of topographic Rossby waves, with shallower water to the right of the current in the Northern Hemisphere where the Coriolis frequency f is positive, and vice versa in the Southern Hemisphere). Its measure is defined by

$$\mathcal{T} = \text{sgn}[f](\hat{\mathbf{z}} \cdot \mathbf{u} \times \nabla h), \quad (1)$$

and its time average near the bottom, denoted by $\bar{\mathcal{T}}_b$, is usually positive. The subscript b denotes a near-bottom value (i.e., within the Monin–Obukhov turbulent layer, outside of any viscous sublayer that would support a no-slip boundary

condition). The overbar is a time average, boldface symbols are horizontal vectors, overlying arrows indicate a 3D vector, $\hat{\mathbf{z}}$ is a unit vertical vector in the upward direction against gravity, and $h(\mathbf{x})$ is the resting depth of the ocean. A unit horizontal vector in the topostrophic direction is

$$\hat{\mathbf{s}} = \text{sgn}[f] \frac{\nabla h}{|\nabla h|} \times \hat{\mathbf{z}}, \quad (2)$$

whence $\mathcal{T} = \hat{\mathbf{s}} \cdot \mathbf{u} |\nabla h|$.

The theory for this phenomenon has its origins in topographic turbulence theory for two-dimensional flow over variable bathymetry (Bretherton and Haidvogel 1976; Salmon et al. 1976; Herring 1977). It shows that random eddying flows evolve to develop a negative correlation between the vertical vorticity, $\zeta = \partial_x v - \partial_y u$, where u and v are the eastward and northward horizontal velocities, respectively, and resting-depth variations, $h - H$, where H is a mean depth. This implies the development of a persistent topostrophic flow that can be described as an eddy-driven mean flow. The rationales for this outcome have variously been given as viscous enstrophy dissipation due to the forward cascade of ζ^2 in two-dimensional turbulence, entropy maximization in the sense of statistical mechanical equipartition of evolutionary end-states, and potential vorticity homogenization through horizontal eddy stirring. Topostrophy is also called the Neptune effect, and Greg Holloway has been a strong advocate for its importance (e.g., Holloway 1987, 1996). For oceanic basins, the most energetic eddies are mesoscale, and the largest $|\nabla h|$

Corresponding author: Esther Capó, estherct@ucla.edu

values occur over continental slopes, seamounts, midocean ridges, and islands, and this is where topostrophy might be most likely to occur; such flows would be in the cyclonic direction on basin edges and anticyclonic around interior bumps. Some striking examples have been reported (Alvarez et al. 1994; Saunders and King 1995; Weijer et al. 2020; Xie et al. 2022), and a climatological dataset from bottom current meters supports the frequent occurrence of topostrophy on slopes (Holloway 2008). In a companion paper (Schubert et al. 2024, manuscript submitted to *Nat. Geosci.*) and in this one, high-resolution, realistic simulations are used to demonstrate the extreme prevalence of topostrophic flows on abyssal slopes.

The second phenomenon focused on in this paper is a prevalent downhill mean flow. If the along-isobath flow is topostrophic, then there is a horizontal drag stress on the bottom, $\tau = \rho C_d |\bar{u}_b| \bar{u}_b$, in the same direction, acting to retard the near-bottom \bar{u}_b . This stress could cause a turbulent bottom (Ekman) boundary layer, whose mean horizontal transport velocity—ignoring the influence of stable density stratification and buoyancy mixing (but see section 7)—is perpendicular to the bottom stress in the downhill direction, i.e., $\bar{u}_b \cdot \nabla h > 0$. Alternatively expressed, the unstratified Ekman layer transport is to the left of the adjacent interior flow in the Northern Hemisphere (and vice versa in the Southern Hemisphere). Furthermore, the mean kinematic bottom boundary condition of no normal flow at a solid boundary is

$$\bar{w}_b = -\bar{u}_b \cdot \nabla h, \quad (3)$$

and this implies that the vertical velocity $\bar{w}_b < 0$ at the bottom.

Care must be taken about details of the vertical profile of the current structure within the boundary layer. In this regard, the third primary phenomenon that we focus on is the mean diapycnal buoyancy mixing associated with these slope flows. An important idealized, one-dimensional (1D) bottom boundary layer (BBL) model (Wunsch 1970; Phillips 1970; Garrett 1990) for the effect of mixing in a stratified fluid with flat buoyancy surfaces in the interior next to a topographic slope has steady solutions with an upslope mean current at the bottom (hence $\bar{w}_b > 0$), a reverse downslope current above, and a retrograde along-isobath mean current in the adjacent interior—all as a consequence of no buoyancy flux through the boundary [ignoring the small geothermal heat flux (Thompson and Johnson 1996)]; see Fig. 1. Stable stratification is expressed as $\partial_z b > 0$, where $b = -g\rho/\rho_0$ is the buoyancy, ρ is the local potential density, and z is the upward coordinate aligned with gravity. The direction of these currents is in contradiction to the topostrophic and Ekman layer expectations in the preceding two paragraphs. This contradiction is resolved in section 7.

The small-scale turbulent buoyancy flux,

$$\bar{\mathcal{B}} = \bar{\mathbf{u}}' \bar{b}', \quad (4)$$

(where primes denote the deviations from mean values that must be defined in each context; in this case, deviations include subgrid-scale fluctuations due to parameterizations and model discretization errors) is “downward” in stable stratification, i.e., toward less buoyant water (e.g., by mixing warm surface water and

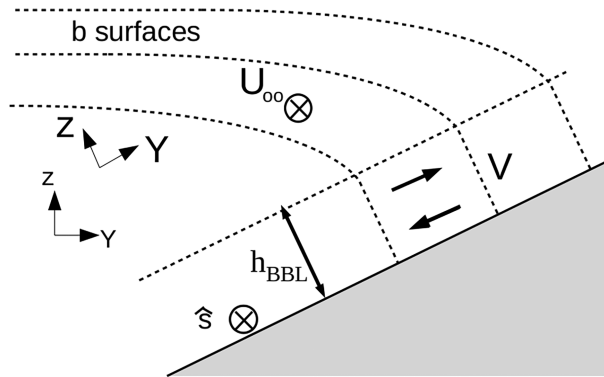


FIG. 1. Sketch of the currents and buoyancy surfaces near a sloping boundary for a topostrophic interior flow when $f > 0$. The Y and Z are the coordinates parallel and perpendicular to the slope, respectively. The h_{BBL} is the BBL thickness, and $V(Z)$ is the cross-slope velocity profile within the BBL; see (15).

abyssal cold water). Extensive microstructure measurements (St. Laurent et al. 2001; Naveira Garabato et al. 2004; Waterhouse et al. 2014; Naveira Garabato et al. 2019) show that in the abyss above “rough” topography, this mixing flux is often largest at a depth somewhat above the sloping bottom due to both boundary layer turbulent mixing and nearby breaking of bottom-generated inertia–gravity waves or topographic wakes. The diapycnal mixing velocity across a buoyancy isosurface is defined by

$$\tilde{\omega} = -\frac{\nabla \cdot \bar{\mathcal{B}}}{|\nabla b|}. \quad (5)$$

Integrated over the horizontal area of a buoyancy surface in the abyss, $\tilde{\omega}$ must be positive both to serve as the upward return flow compensating polar sinking in the global thermohaline circulation and to account for the water mass transformation of less buoyant into more buoyant water. Invoking the slope buoyancy-mixing BBL model cited above and the observed vertical structure of diapycnal mixing near topography (e.g., Ferrari et al. 2016; McDougall and Ferrari 2017; Callies 2018; Holmes and McDougall 2020; Drake et al. 2022; Baker et al. 2023), it is hypothesized that most of the dominant positive $\tilde{\omega}$ occurs in the BBL next to the slopes and weaker negative values occur in the interior, with a spatially inhomogeneous pattern concentrated near topographic slopes. This is a modern revision of the older conceptions of positive w and $\tilde{\omega}$ more homogeneously spread throughout the abyssal interior (Stommel 1958; Munk 1966).

The intersection of these processes occurs principally in the mean buoyancy balance:

$$\partial_t \bar{b} = -\bar{\mathbf{u}} \cdot \nabla \bar{b} - \nabla \cdot \bar{\mathcal{B}}, \quad (6)$$

$$= -\bar{\mathbf{u}} \cdot \nabla \bar{b} + \tilde{\omega} |\nabla b| \approx 0, \quad (7)$$

especially near bottom slopes. The mean and eddy buoyancy advection approximately balances the small-scale mixing, i.e., their tendencies must have opposite signs in equilibrium.

In this paper, we partially synthesize these processes guided by realistic regional simulations, but leaving the full characterization

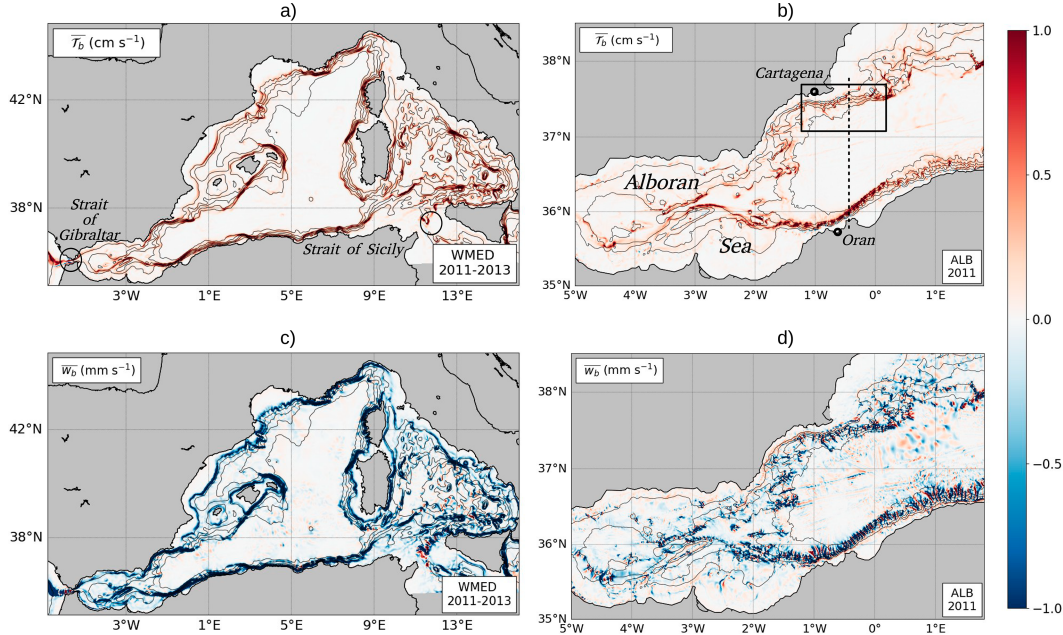


FIG. 2. (a),(b) Time-averaged \bar{T}_b and (c),(d) \bar{w}_b in the (a),(c) WMED and (b),(d) Alboran simulations. Bathymetry is contoured in black every 500 m. The black box in (b) frames the Cartagena subdomain analyzed in Fig. 4 et seq., and the dashed line indicates the section shown in Fig. 10. Locations of interest are labeled in (a) and (b).

of the upward branches of the thermohaline circulation to future global simulations. Our findings are that topographic flows are very common and that \bar{w} and $\tilde{\omega}$ are mostly negative along the abyssal slopes, but with sign reversals toward the interior. Our focus is on the abyss because there can be many competing influences on the mean currents in the upper ocean (e.g., the wind-driven western boundary current in a subtropical gyre); whereas, mesoscale eddies are ubiquitous and are often the dominant influence on the mean currents in the abyss (e.g., Rhines and Holland 1979). We use the western Mediterranean Sea to illustrate this behavior. Schubert et al. (2024, manuscript submitted to *Nat. Geosci.*) is a companion paper showing that this is common throughout the Atlantic and Pacific Oceans, and J. Gula et al. (2024, unpublished manuscript) explain the method of diagnosing \mathcal{B} in a terrain-following coordinate model (as used here), inclusive of both explicitly parameterized mixing and the contribution from model discretization errors.

The organization of the paper is as follows. The general circulation of the western Mediterranean Sea is summarized in section 2; the simulation specifications are in section 3; the near-slope circulation results are in section 4; the mean along-isobath momentum $\hat{s} \cdot \bar{u}$ and buoyancy \bar{b} balances are diagnosed in sections 5 and 6; a simple 1D BBL model combining diapycnal mixing and a topographic interior flow is in section 7; and the results are further discussed and summarized in sections 8 and 9.

2. Western Mediterranean circulation

Topography is a widespread phenomenon (Holloway 2008; Schubert et al. 2024, manuscript submitted to *Nat. Geosci.*). The analysis here is conducted in the western Mediterranean

basin, with a particular focus on the Alboran Sea, partly taking advantage of existing simulations and previous analyses (Capó et al. 2021; Capó and McWilliams 2022; Capó et al. 2023).

The western Mediterranean Sea is a semienclosed basin located between the Strait of Gibraltar, 36°N–5.5°W, and the Strait of Sicily, 37°N–12°E (Fig. 2a). The region is characterized by a complex bathymetry shaped by numerous capes, seamounts, ridges, and islands of different shapes and sizes. While the interior of the basin is relatively flat, with an averaged depth not exceeding 3000 m, the continental and island/ridge margins are characterized by steep slopes, often shaped with narrow, deep canyons. The Alboran Sea is the transitional area between 5.5° and 1°W that connects the western Mediterranean Sea with the Atlantic Ocean through the narrow Strait of Gibraltar (Figs. 2a,b).

In the upper 150–200 m, the large-scale circulation in the Alboran Sea is mainly driven by the incoming Atlantic jet, a strong fresh, surface current with velocities of $O(1)$ m s⁻¹ forced by a strong surface pressure gradient between both sides of the strait and modulated by the tides affecting the Atlantic side. This jet flows along the basin shaping the quasi-permanent Western Anticyclonic Gyre and an intermittent, less intense Eastern Anticyclonic Gyre (Viúdez et al. 1996; Vargas-Yáñez et al. 2002). To the east, the meeting of the Atlantic fresh current with the resident salty Mediterranean water generates a strong surface density (mainly salinity) contrast, commonly named the Almería–Oran Front (Tintore et al. 1988; Allen et al. 2001). The Atlantic jet exits the Alboran Sea and flows eastward along the African coast toward the Strait of Sicily as the Algerian Current. The Mediterranean thermohaline

circulation transforms the incoming fresh Atlantic water into saltier water, which leaves the basin toward the Atlantic Ocean through the Strait of Gibraltar in the form of Levantine Intermediate Waters, within a 200–600-m depth range on average, and deep Mediterranean Water below. These currents follow a complicated path that is highly constrained by the shape of topography: a major branch of the Levantine Undercurrent flows along the Spanish margin toward the Strait, while the denser deep Mediterranean Water occupies the central (and deepest) part of the basin and finally flows toward the Strait along the African slope (Sánchez-Garrido and Nadal 2022). The influence of subbasin-scale interactions between oceanic eddies and bottom topography in the western Mediterranean Sea was first investigated in Alvarez et al. (1994). By testing a parameterization of the eddy-topography interaction through various numerical experiments, their study suggested that topographic stress could play a significant role in driving circulation at both basin and subbasin scales.

The western Mediterranean Sea exhibits a high degree of eddy variability, manifested in its boundary currents, surface density fronts, pycnocline depth variations, large and rapid vertical parcel displacements, topographic vorticity generation, and abyssal currents, e.g., partly as shown in the recent Coherent Lagrangian Pathways from the Surface Ocean to Interior (CALYPSO) experiments (Mahadevan et al. 2020).

3. Mediterranean simulations

We use two realistic simulations with the Regional Oceanic Modeling System (ROMS) (Shchepetkin and McWilliams 2005) and different spatial grid resolutions: 1) the western Mediterranean (WMED) basin with horizontal $dx = 1500$ m and 60 σ levels in the vertical [with stretching parameters $\theta_s = 7$ and $\theta_b = 5$ near the surface and the bottom, respectively, following Lemarié et al. (2012)], and 2) the nested subdomain for the Alboran Sea (ALB) with $dx = 500$ m, 140 σ levels, and $\theta_s = \theta_b = 7$. WMED was calculated using Coastal and Regional Ocean Community (CROCO), a modeling system built upon ROMS with a numerical kernel close to the University of California, Los Angeles (UCLA), version of the ROMS model (Shchepetkin and McWilliams 2009; <http://www.croc-ocean.org>). ALB was calculated using the UCLA-ROMS version of the model (<https://github.com/CESR-lab/ucla-roms.git>). The two codes have enough of a common heritage that their solution behaviors are similar.

ROMS is a split-explicit, 3D free-surface oceanic model that solves the hydrostatic primitive equations for momentum, temperature, and salinity using the Boussinesq approximation and hydrostatic vertical momentum balance (Shchepetkin and McWilliams 2005). Horizontal advection is based on a modified version of the upstream third-order scheme, which is split into a fourth-order centered advection and a rotated biharmonic diffusion with grid-dependent diffusivity satisfying the Peclet constraint (Marchesiello et al. 2009; Lemarié et al. 2012). To avoid numerical instabilities, the algorithm for vertical advection of momentum combines a high-order explicit scheme with an implicit one, which mitigates the vertical Courant–Friedrichs–Lewy restriction (Shchepetkin 2015). Vertical

advection of tracers is performed using a fourth-order Akima scheme.

In both configurations, the top and bottom boundary layers are well resolved using a K -profile parameterization (KPP) for the turbulent mixing (Large et al. 1994). With this scheme, the mixing coefficients reach maximum values in the middle of the layers, decreasing to minimal background values within the interior, except where the Richardson number, Ri , becomes small. Bottom drag is parameterized using the quadratic law, $\tau = \rho_0 C_D \|\mathbf{u}_b\| \mathbf{u}_b$, where ρ_0 is the reference density, \mathbf{u}_b is the horizontal velocity in the bottom layer, and C_D is a drag coefficient. We use the logarithmic formulation for $C_D = [k/\log(\Delta z_b/z_r)]^2$, where $k = 0.41$ is the von Kármán constant, Δz_b is the thickness of the bottom layer, and z_r is the roughness scale, set to 1 cm.

Bathymetry for both domains is obtained from the SRTM30_PLUS_V11 global dataset (Becker et al. 2009). A steepness factor $r < 0.2$ is applied to realistic topography to limit pressure gradient errors. An additional smoothing with a radius of 4-km half-width is also applied to the grid in the ALB solution.

Realistic atmospheric forcing for the WMED solution is derived from the NCEP–CFSR dataset at 0.2° resolution. Wind velocity, temperature, and humidity fluxes and shortwave and longwave radiation fluxes feed the model at hourly time steps, and river inflow is derived from a climatological dataset. The initial and boundary conditions for WMED are interpolated from the Copernicus Marine Service global ocean forecasting system (Lelloucou et al. 2018), providing a realistic representation of the western Mediterranean Sea in the mesoscale range (Mason et al. 2019). This simulation was run for 4 years, 2010–11, with a spinup period of approximately 3 months, although the first year is excluded from the analysis. Capó (2020) provides a detailed description of this solution, including validation and data analysis.

The corresponding atmospheric forcing for ALB is obtained from the fifth major global reanalysis produced by ECMWF (ERA5) at hourly time steps (Hersbach et al. 2020). The initial state and boundary conditions for ALB are obtained from WMED, and the simulation is initialized in December 2010, 11 months after WMED initialization to ensure sufficient spinup of the latter.

Boundary conditions consist of a Flather-type scheme for the barotropic mode and an Orlansky-type scheme for baroclinic velocity and for tracers, following the nesting procedure described in Mason et al. (2010).

Neither of the simulations analyzed here is forced with tides. Although internal tides play a crucial role in enhancing mixing over abyssal slopes in the oceans, these are not the sole contributors in our study region and are not so essential for our analysis. Lee waves, topographic wakes, submesoscale instabilities, and interactions with mesoscale eddies also play important roles in enhancing mixing along abyssal slopes (Legg 2021; Mashayek et al. 2024), and these processes occur in our solution at submesoscale resolution despite the absence of tidal forcing. While the tidal effect is important as part of the Atlantic inflow through the Strait of Gibraltar, tidal amplitudes decay toward the interior of the basin, and the effect of topographic wakes, lee waves, and other instability sources

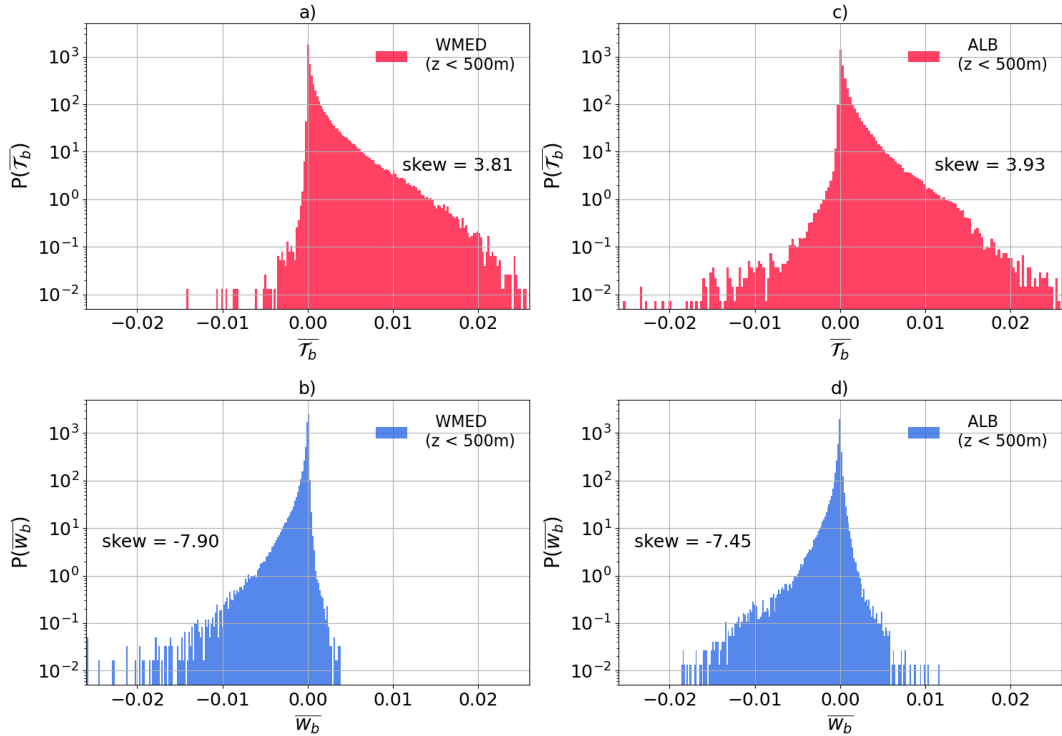


FIG. 3. PDFs for the bottom fields, (a),(c) \bar{T}_b (m s^{-1}) and (b),(d) \bar{w}_b (m s^{-1}), for time-averaged values at each location in the (a),(b) WMED and (c),(d) Alboran simulations (m s^{-1}). Only locations with resting depths $h \geq 500$ m are included. The predominance of negative \bar{w}_b and positive \bar{T}_b is evident, e.g., in the indicated values of skewness.

can be as relevant as internal tides in enhancing mixing near abyssal slopes in the Mediterranean Sea. Comparisons with tidal solutions show modest differences in the topostrophy and downhill mean flows that are the primary focus of this paper (section 4).

The ALB simulation is based on a previous solution with an identical configuration that included tidal forcing, ALB_T, and is extensively validated and analyzed in Capó (2020). The new ALB solution presented here shows consistency with the parent WMED and with ALB_T. ALB validation entailed a comparison of the 3D flow structures, temperature and salinity fields, and the analysis of time series of area-averaged kinetic energy and local sea surface height throughout the domain. The latter are consistent with those obtained from the parent WMED and serve to determine the spinup period required until the model stabilizes. The absence of tidal forcing facilitates rapid stabilization, which is achieved after 2 weeks. For greater reliability, the first 2 months of the ALB simulation are excluded from the analyzed period.

The results presented in this paper, if not otherwise indicated, are obtained from daily averaged fields of the last 3 years of the WMED solution (2011–13) and from the last year of ALB (February 2011–January 2012).

4. Abyssal topostrophy and downhill flow

In this section, we examine the first two phenomena exposed in section 1: topostrophy, \bar{T} , and downhill bottom flow,

\bar{w}_b , using our two simulations in the western Mediterranean, WMED, and ALB and the definitions in (1)–(3). Figure 2 shows these fields over the whole domains of WMED and ALB. As anticipated, \bar{T}_b is primarily positive and \bar{w}_b is primarily negative. Recall that both quantities are weighted by ∇h and thus tend to be largest over slopes. Not all slope regions have these signatures, but there is very little evidence of opposite signs with significant magnitude.

A more complete view is provided by the probability distribution functions (PDFs) for these fields at locations with resting depths ≥ 500 m (Fig. 3). There are many small values due to locations with small $|\nabla h|$, but the PDFs are highly skewed in both their bulk and tails.

The ALB simulation has a significantly increased spatial bathymetry and grid resolution compared to WMED (section 3). It therefore exhibits greater variability in these measures, especially in \bar{w}_b . Partly, this is expressed in dipole patterns over bumps and ridges and along the sides of submarine canyons that interrupt the primary continental slopes. In particular, abundant submarine canyons interrupt the Spanish slope between 1.2°W and 0.2°E (the Cartagena subregion delimited in black in Fig. 2) and the African margin between 2°W and 1.5°E (the path of the eastward Algerian Current). It has been widely shown from both numerical simulations and observations that currents flowing across canyons induce opposite-signed \bar{w}_b values on the upstream (negative w) and downstream (positive w) sides (Klinck 1996; Flexas et al. 2006; Spurgin and Allen 2014) with reversed w signs for flow over bumps. In combination with

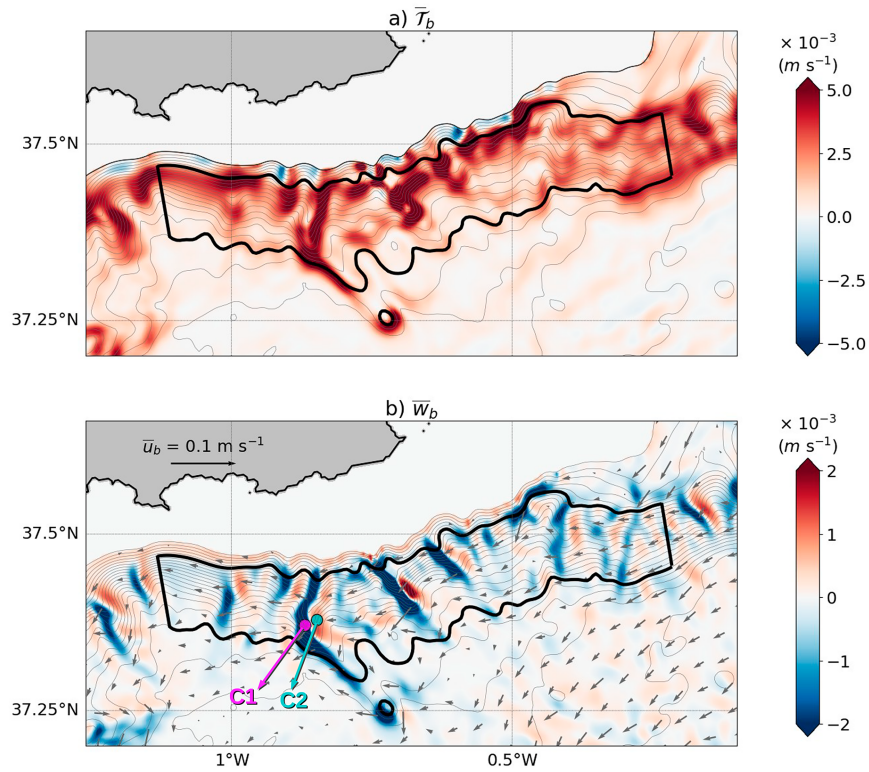


FIG. 4. A zoom into the Cartagena region depicted within the black box in Fig. 2b for time-averaged (a) \bar{T}_b and (b) \bar{w}_b (colors) and \bar{u}_b (vectors) for resting depths ≥ 500 m in the ALB simulation. Bathymetry is contoured in black every 100 m. The thick black line defines the subregion for the along-isobath averages in Fig. 5 et seq. The points C1 and C2 in (b) mark two representative locations on opposite sides along a ridge, used in Fig. 7 to illustrate the local flow vertical profiles.

prograde slope flow, this local canyon effect results in a net downhill transport. These features are shown in detail in Fig. 4 for the Cartagena subregion. The prevailing topographic, downhill flow in this region is part of the Levantine and deep Mediterranean Undercurrent that crosses the Alboran Sea westward toward the Strait of Gibraltar. We have chosen to focus on the Cartagena region, both here and below, as one that seems at least not atypical from the perspective of Fig. 2. No doubt there are meaningful regional differences, but based on our present level of exploration, the behavior of Cartagena is representative of the structure and dynamics of abyssal slope flows.

To better discern the behavior associated with the primary abyssal slope, we average over the local flow structures evident in Fig. 4 by averaging in the \hat{s} direction (i.e., along isobaths) within the thick black subregion there. This is done by binning all grid points along the slope with a discretization interval of 40 m in the local depth.

The result is denoted by angle brackets, $\langle \cdot \rangle$, and we show cross sections in vertical height z and horizontal distance across the mean slope η (increasing toward deeper water), e.g., $\langle \bar{T} \rangle(\eta, z)$ and $\langle \bar{w} \rangle(\eta, z)$ in Fig. 5. Topostrophy is positive for hundreds of meters above the slope, with maximum values at ~ 1200 -m depth, and the averaged $\langle \bar{w} \rangle$ profile shows a

predominance of strong downwelling within the lowest ~ 80 m with weaker upwelling above and even weaker downwelling further into the interior.

Topostrophy and vertical velocities near the bottom have been also examined in a solution similar to ALB but forced with tides (Capó et al. 2021, 2023), with very similar results in the distribution of positive \bar{T} and predominantly negative \bar{w}_b , with slightly increased values due to tidal effects on bottom velocities. Further ROMS simulations in the Atlantic and Pacific Oceans examined in Schubert et al. (2024, manuscript submitted to *Nat. Geosci.*)—with different topographic smoothing, horizontal resolution, and time averaging over several time scales—show the same overall predominance of prograde flows, with positive topostrophy and negative vertical velocity near the abyssal slopes. Their work includes diagnostics from a multitude of current-meter measurements that support the hypothesis of prevalent, widespread prograde currents and downhill flows.

5. Mean momentum

To investigate the various forces sustaining the topographic flow, in this section, we analyze the momentum balance in our solution, with a focus on the Cartagena slope.

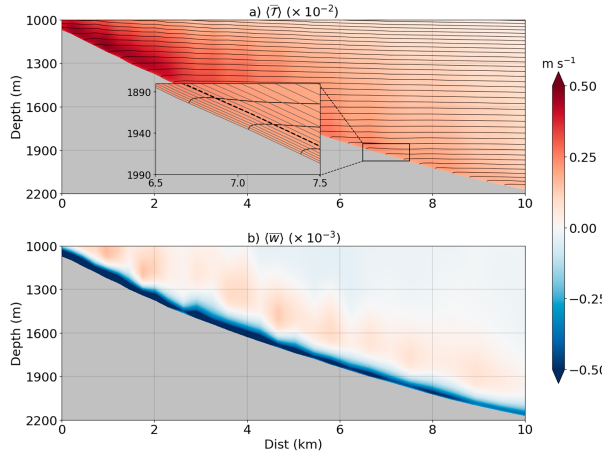


FIG. 5. Time-averaged and along-isobath-averaged cross sections on the Cartagena slope (i.e., within the thick black line in Fig. 4, between 0.25° and 1.1°W) in the ALB simulation: (a) topography $\langle \bar{T} \rangle(\eta, z) (\times 10^{-2})$ and (b) vertical velocity $\langle \bar{w} \rangle(\eta, z) (\times 10^{-3})$, both referenced to the color bar values on the right side. The η is a horizontal coordinate in the cross-isobath direction, increasing toward deeper water. Isopycnals are contoured in black in (a), and the inset box shows in detail the tilting of isopycnals perpendicular to the sloping floor, consistent with zero buoyancy flux at the boundary. Also, in the inset, the dashed black line represents the mean BBL depth (as diagnosed in the model from KPP), and the local configuration of the sigma levels is contoured in gray, showing that the vertical resolution of the model increases significantly toward the bottom.

Then, we explore the eddy-driven nature of the widespread mean prograde flow by decomposing the advective forcing term into contributions from the mean flow, transient eddies, and standing eddies. Finally, an analogous decomposition of the time-averaged kinetic energy (KE) highlights the prominence of eddies as a principal characteristic.

a. Along-isobath momentum balance and bottom drag

The time-averaged momentum balance in the along-isobath direction is

$$\hat{\mathbf{s}} \cdot \partial_t \bar{\mathbf{u}} \approx 0 = +\underbrace{\hat{\mathbf{s}} \cdot (\bar{\mathbf{u}} \cdot \nabla) \bar{\mathbf{u}}}_{\text{ADV}} - \underbrace{\hat{\mathbf{s}} \cdot \nabla \bar{\phi}}_{\text{PGF}} - \underbrace{f \hat{\mathbf{s}} \cdot \hat{\mathbf{z}} \times \bar{\mathbf{u}}}_{\text{COR}} + \underbrace{\hat{\mathbf{s}} \cdot \bar{\mathbf{F}}}_{\text{VMIX}}, \quad (8)$$

where VMIX is the parameterized vertical mixing in ROMS described in section 3. The other right-side tendency terms are advection (ADV) of along-isobath momentum, along-isobath pressure-gradient factor (PGF), and Coriolis (COR) forces. This balance is diagnosed online and then averaged in time and along isobath. Additional terms in the discretized ROMS momentum equations are negligible in our time-averaged momentum balance (8); these include numerical dissipation by the horizontal advection scheme and a rectification that results from the coupling of the 2D–3D barotropic–baroclinic, split-explicit time-stepping scheme (Shchepetkin and McWilliams 2005).

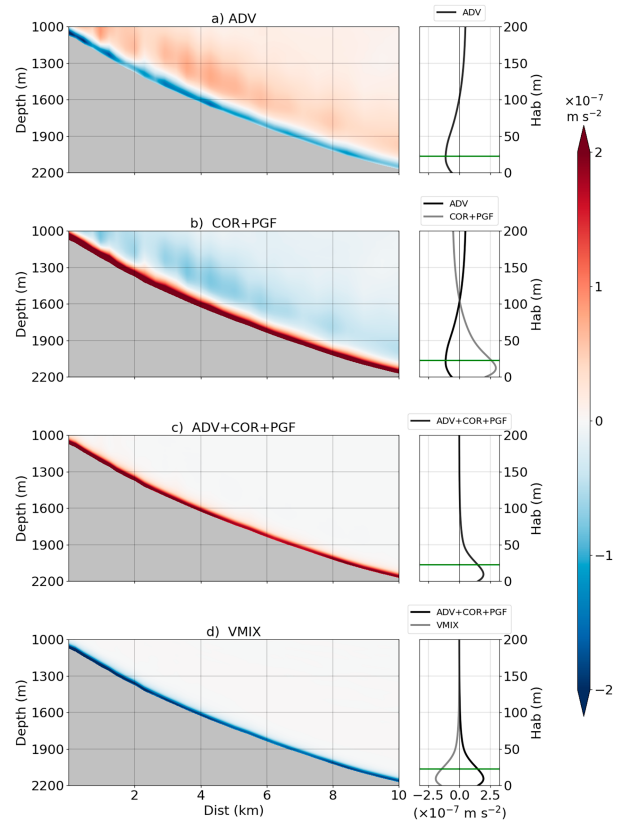


FIG. 6. (left) Time-averaged and along-isobath-averaged cross sections on the Cartagena slope for the along-isobath momentum balance (8) in the ALB simulation: (a) $\langle \text{ADV} \rangle$, (b) $\langle \text{PGF} + \text{COR} \rangle$, (c) $\langle \text{ADV} + \text{PGF} + \text{COR} \rangle$, and (d) $\langle \text{VMIX} \rangle$. (right) The 1D profiles show the corresponding area-averaged terms for the lower 200 m, as a function of height above the bottom ($\text{Hab} = h + z$). While in the interior (100 m and above), the balance is between ADV, COR, and PGF; in the lower tens of meters (including the averaged BBL delimited by the green line), the accelerating combination of COR, ADV, and PGF is compensated by the retarding effect of bottom drag expressed in the vertical mixing term.

Figure 6 shows the momentum balance terms in various combinations. On the left panels, the geostrophic balance is hidden in COR + PGF, leaving behind a residual that is mostly balanced by ADV, especially in the interior away from the slope. VMIX is small except within the BBL, where it reflects the retardation of the topographic current by bottom drag stress and its vertical redistribution by momentum mixing. Because the force balances exhibit continuity along the slope, the slope-averaged profiles shown in the right panels as a function of height above the bottom are representative of the balances in the BBL and adjacent interior. These balances broadly support the ideas of conservative dynamics in the interior and an Ekman-like balance in the BBL (but see section 7).

b. Eddy-driven topographic flow

To explore the influence of the eddies in driving the topographic flow, we now decompose the advective term ADV

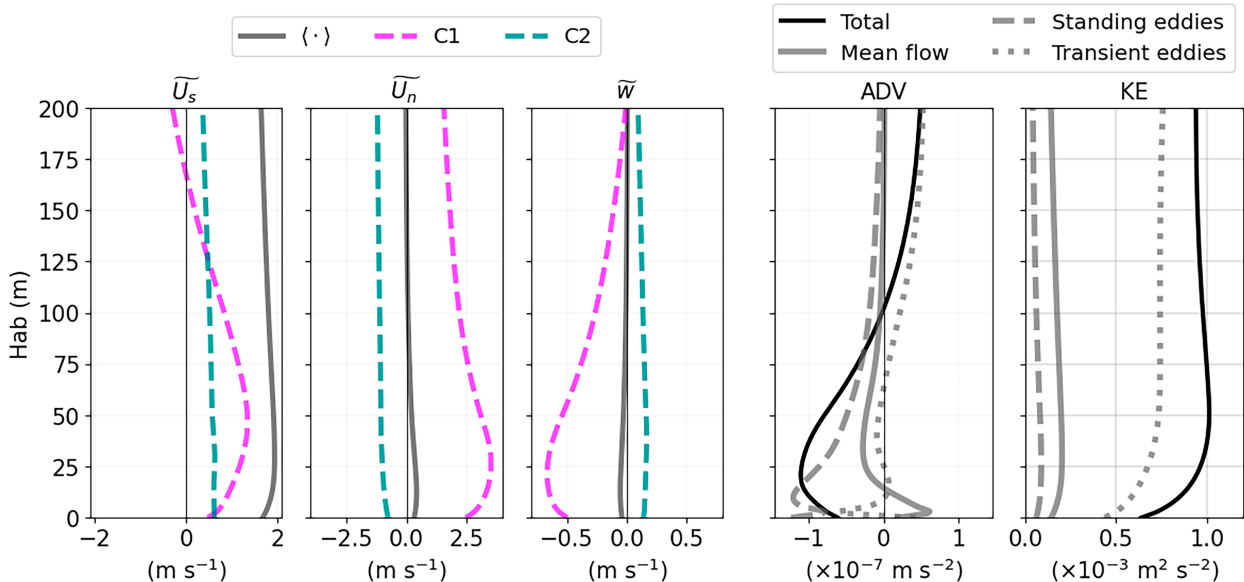


FIG. 7. The left three panels show time-averaged profiles of the along-slope (\widetilde{U}_s), cross-slope (\widetilde{U}_n), and vertical (\widetilde{w}) velocities, both for the area-averaged flow in the Cartagena region (dark gray) and for two specific canyon locations shown in Fig. 4, C1 and C2 (pink and blue shaded lines, respectively). While the flow is generally topographic ($\widetilde{U}_s > 0$), it is oriented uphill on the upstream side of a bump (C2, with $\widetilde{U}_n > 0$ and $\widetilde{w} > 0$) and downhill on the downstream side (C1, with $\widetilde{U}_n > 0$ and $\widetilde{w} < 0$). The right two panels show the time- and area-averaged profiles of the decomposed advective term in the momentum balance (ADV) and KE separated into the total (black), mean (gray), standing eddy (dashed gray), and transient eddy (dotted gray) components. In the lower 100 m, ADV is dominated by standing eddies and by the transient eddy component above, while transient eddies are also the principal source of KE at all levels.

into the contributions of the mean flow and eddy components. Given that the flow structure near the slope in this region is highly modulated by topography (Fig. 4), we chose to make a decomposition of the flow as follows: a flow component $u_i(\mathbf{x}, t)$ at a given location \mathbf{x} and time t can be written as

$$u_i(\mathbf{x}, t) = \langle \overline{u}_i \rangle + \widetilde{u}_i + u'_i, \quad (9)$$

where $\langle \overline{u}_i \rangle$ is the mean flow, defined here as the time and along-isobath average; $\widetilde{u}_i = \overline{u}_i - \langle \overline{u}_i \rangle$ is the standing (or stationary) eddies; and $u'_i = u_i - \overline{u}_i$ is the transient eddies. The standing eddy component accounts for the persistent circulation patterns that, in this particular case, are mainly caused by the interaction of the flow with topographic irregularities, such as canyons and bumps; the transient eddy component includes temporary eddies that are typically generated by instabilities in the flow field, such as ageostrophic shear instabilities and geostrophic barotropic or baroclinic instabilities.

Using (9), the time-averaged advective term in the momentum equation can be written as

$$\begin{aligned} \overline{(\mathbf{u} \cdot \nabla) \mathbf{u}} &= \underbrace{\langle (\overline{\mathbf{u}} \cdot \nabla) \langle \mathbf{u} \rangle \rangle}_{\text{Mean}} + \underbrace{\langle (\overline{\mathbf{u}} \cdot \nabla) \widetilde{\mathbf{u}} + (\widetilde{\mathbf{u}} \cdot \nabla) \langle \mathbf{u} \rangle + (\widetilde{\mathbf{u}} \cdot \nabla) \widetilde{\mathbf{u}} \rangle}_{\text{standing eddies}} \\ &+ \underbrace{\langle (\mathbf{u}' \cdot \nabla) \mathbf{u}' \rangle}_{\text{transient eddies}}. \end{aligned} \quad (10)$$

where the first term on the right side is the contribution of the mean flow, the next three terms represent the contribution of the standing eddies, and the last term represents the advection

by transient eddies. By projecting (10) onto the along-isobath direction \hat{s} , we obtain the corresponding mean, standing eddy, and transient eddy contributions to the ADV term in (8).

Using an analogous decomposition, the total time-averaged KE is

$$\frac{1}{2} \overline{\mathbf{u}^2} = \underbrace{\frac{1}{2} \langle \overline{\mathbf{u}} \rangle^2}_{\text{Mean}} + \underbrace{\widetilde{\mathbf{u}} \cdot \langle \overline{\mathbf{u}} \rangle}_{\text{standing eddies}} + \underbrace{\frac{1}{2} \widetilde{\mathbf{u}}^2}_{\text{transient eddies}}, \quad (11)$$

where the first term on the right side is the KE of the mean flow; the next two terms constitute the eddy KE (EKE) stored in standing eddies; and the last term accounts for the EKE of the transient eddy flow.

The advection and KE results of this flow decomposition are summarized in Fig. 7. To highlight the relevant influence of topographic interaction in driving the abyssal sloping currents and to provide an idea of its vertical extent, in the first three panels, we compare the time-averaged standing eddy component of the along-isobath \widetilde{U}_s , the cross-isobath \widetilde{U}_n , and the vertical \widetilde{w} components of the flow for three cases: the area-averaged flow (dark gray line) and at two representative locations at both sides of a bump, C1 and C2 (pink and blue dashed lines, respectively; see Fig. 4). In all situations, the along-isobath component is topographic, while the cross-isobath and vertical components are in opposite directions at both sides of the bump and locally much more intense than the widespread downhill flow.

Figure 7 also shows that standing eddies dominate the mean advection of momentum in the lower ~ 80 m, while transient eddies are the dominant contribution above. Transient eddies

dominate the mean KE at all depths near the slope. These results provide evidence of the eddy-driven nature of the topographic flow in our abyssal sloping currents. However, a more complete analysis of abyssal eddy dynamics, perhaps as a function of spatial scale, is needed to explain the widespread topographic outcome. Because the statistical stationarity of the solution is imperative in such analysis, we choose to defer this until we can achieve a higher-resolution simulation with a longer time-averaging period. In lieu thereof, the along-isobath averaged momentum balance that we present here is broadly in line with previous studies that show the turbulent character of the forces driving the mean along-isobath flow within the BBL (Molemaker et al. 2015; Chen et al. 2021; Stewart et al. 2024). Naveira Garabato et al. (2019) and Spings et al. (2021) present observational evidence for the manner in which topographically localized turbulence is generated through submesoscale overturning instabilities in the near-boundary flow [e.g., symmetric and centrifugal instabilities; Wenegrat and Thomas (2020)] that arise in the measured topographic and downhill mean slope flow. In section 1, some further comments are made about present theoretical ideas about the cause of topostrophy. Such arguments are clearest in barotropic or isopycnal-layer models, whereas the ocean (and ROMS) is continuously stratified. Some attempts have been made to extend the theory to three dimensions (Merryfield and Holloway 1999; Venaille 2012) but not yet with much generality.

From a horizontal momentum-balance perspective, an important distinction is what averaging framework is chosen to encompass a region of complex topography. Beyond time averaging, one can choose between a mean horizontal direction (e.g., an average $\langle \hat{s} \rangle$ over the broad slope area) or a local along-slope direction (\hat{s} , as here). Stewart et al. (2024) analyze idealized simulations of corrugated slope flows and find that the near-bottom topostrophy-accelerating force is PGF with a mean alongshore average, whereas the same simulations show ADV acceleration using an along-isobath average, consistent with our finding here. In more realistic simulations of the California Undercurrent, another topographic slope flow, averaging more broadly in the along-isobath direction, implicates a PGF acceleration cause (Molemaker et al. 2015; Chen et al. 2021). Because ADV and PGF are closely related quantities in incompressible fluid dynamics that manifest turbulent behaviors, there is no contradiction in these different diagnostic perspectives.

The choice of an averaged direction for the momentum balance might be simple for a unidirectional flow past an isolated bathymetric feature, but it can become ambiguous for complex currents and multiscale topography as in these simulations. This led us to choose the local \hat{s} . Another important issue is whether the direction should be spatially smoothed, i.e., on what spatial scales is topostrophy more likely to occur? We have not yet investigated this but notice that the general pattern of \bar{T} is quite similar in the WMED and ALB simulations with different grid resolutions by a factor of 3 (Fig. 2).

6. Near-slope buoyancy balance and diapycnal mixing

The widespread negative \bar{w}_b fields observed in the western Mediterranean simulations, as well as in the Atlantic and

Pacific solutions presented in Schubert et al. (2024, manuscript submitted to *Nat. Geosci.*), do not match the behavior expected by the 1D BBL model by Garrett (1990), which predicts upslope mean current at the bottom ($\bar{w}_b > 0$) and negative topostrophy. In this section, we analyze the mean BBL buoyancy balance (7) for the ALB solution to show the vertical structure near the slope. The contradiction between our results and the predictions in Garrett (1990) is further examined in an alternative 1D BBL model in section 7.

The buoyancy balance terms in (7) are obtained in ROMS from the online-diagnosed advection and mixing terms in the balances for potential temperature T and salinity S . They are combined into buoyancy fluxes with a local linearization of the equation of state (EOS):

$$\delta b = -\frac{g}{\rho_0}(-\alpha\delta T + \beta\delta S), \quad (12)$$

where δ denotes the local differential change in the balance terms and $\alpha = \partial\rho/\partial T$ and $\beta = \partial\rho/\partial S$ are the local density expansion coefficients. For example, for advection,

$$\mathbf{u} \cdot \nabla b = -\frac{g}{\rho_0}(-\alpha \mathbf{u} \cdot \nabla T + \beta \mathbf{u} \cdot \nabla S), \quad (13)$$

with an analogous combination in $\nabla \cdot \bar{\mathcal{B}}$ for the mean T and S mixing terms. ROMS uses a nonlinear EOS that corresponds to the UNESCO formulation as derived by Jackett and McDougall (1995) that computes in situ density as a function of potential temperature, salinity, and pressure, which is approximated as a function of depth. This EOS is then “stiffened” by a split into an adiabatic and a compressible part to reduce pressure-gradient errors associated with the nonlinear compressibility effect (Shchepetkin and McWilliams 2011).

The method of analyzing in ROMS the total buoyancy mixing term, $-\nabla \cdot \bar{\mathcal{B}}$, due both to the explicit subgrid-scale parameterization and model discretization errors, is presented in J. Gula et al. (2024, unpublished manuscript).

The occurrence of a mean downhill slope flow gives an expectation that the advective tendency in (7) will be positive, i.e., acting to increase the buoyancy. Of course, advection is three-dimensional and time-varying, including by the mean current and by the standing and transient eddies. Assuming a nearly stationary state with negligible net buoyancy tendency, if the advective tendency is positive, then the necessary balancing mixing tendency will be negative, acting to decrease the buoyancy through a divergent \mathcal{B} flux. Because $\tilde{\omega}$ in (5) has the same sign as the mixing tendency term, this is a wide layer with diapycnal downwelling along the slope, contrary to the arguments in Ferrari et al. (2016), etc. This difference is explained through the use of an idealized boundary layer model in section 7.

Figure 8 shows the time-averaged and along-isobath-averaged buoyancy balance for the Cartagena region, and a detail of the lowest 100 m over the slope is shown in Fig. 9. As anticipated from $\bar{T}_b > 0$ and $\bar{w}_b < 0$ in section 1, the buoyancy advection tendency is positive, and the mixing tendency is negative in the

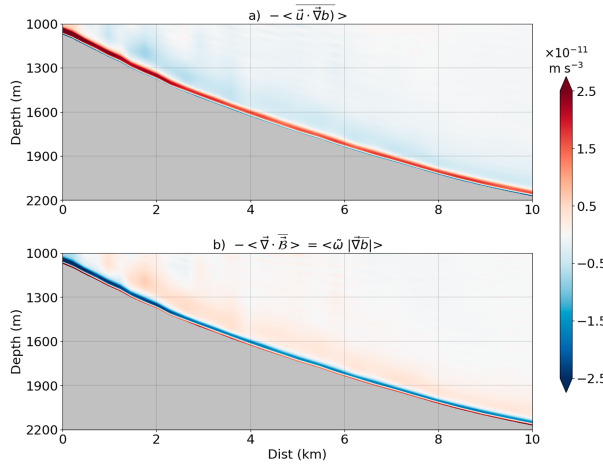


FIG. 8. Time-averaged and along-isobath-averaged cross sections on the Cartagena slope for the buoyancy balance (7) in the ALB simulation: (a) ADV and (b) mixing.

middle and upper parts of the boundary layer, with sign reversals in the adjacent interior.

However, within a thin layer just a few meters thick along the slope, there is a negative advective tendency, contrary to the $\bar{w}_b < 0$ expectation. This is a subtle effect of eddy buoyancy advection as demonstrated in Fig. 12 and further explained in section 7. The expanded scale in the BBL close to the slope in Fig. 9 shows that the vertical sign reversals occur well inside the BBL, accompanied by a further sign change higher in the interior. Here, we are using a transformed vertical coordinate, the height above the bottom, $Hab = z + h$.

The positive sign of $\tilde{\omega}$ in (5) in the outer part of the BBL and above means diapycnal upwelling. Its sign reversal is consistent with the sign reversal of the cross-isobath velocity profile in the 1D topographic boundary layer model [i.e., $V(Z)$ in Fig. 1 and $V'(Z)$ in Fig. 13 below]. Thus, our results are consistent with the idea that much, maybe most, of the mixing-induced abyssal upwelling in the global thermohaline circulation may be happening near the major topographic slopes, even if it is not confined to a thin bottom boundary layer immediately above the slope.

While the tracer mixing in our simulations is prescribed by the turbulence parameterization (with the vertical eddy diffusivity κ_v derived from the KPP scheme; section 3), in practice, mixing of temperature and salinity in the model can additionally arise from implicit contributions from the horizontal and vertical advection schemes as well as other discretization errors, in particular, where currents and T and S gradients are large. The resulting nonadvective T and S fluxes will result in an “effective” diffusivity κ_{eff} that can differ from the prescribed vertical diffusivity κ_v (J. Gula et al. 2024, unpublished manuscript) and that is not confined only to a thin bottom boundary layer immediately above the slope. In the context of abyssal slope currents, bottom-intensified mixing due to breaking inertia–gravity waves and topographic wakes is an important phenomenon (section 1) even beyond the turbulent mixing in the BBL. With the horizontal grid resolution of

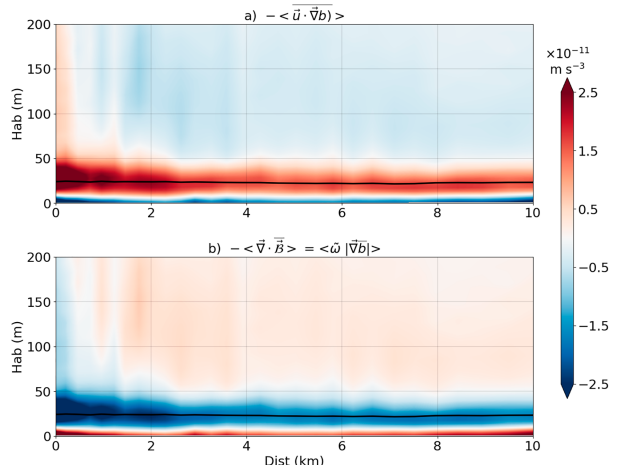


FIG. 9. A zoom of the fields in Fig. 8 in coordinates of height above the bottom $Hab = z + h$ and cross-slope horizontal distance η . The black thick line is the mean boundary layer height (as diagnosed in the model from KPP).

$dx = 500 \text{ m}$ in the ALB simulation (section 3), we can expect an incomplete representation of this adjacent interior mixing apart from what occurs in κ_v due to the small Richardson number in the model-resolved shear and stratification (Large et al. 1994). Nevertheless, we can assess both it and the effective diapycnal mixing in our solution by evaluating the prescribed κ_v with the diagnosed κ_{eff} . The diagnostic method for the latter is presented in J. Gula et al. (2024, unpublished manuscript) and illustrated there with ROMS simulations for the Atlantic Ocean.

By definition, κ_{eff} is obtained by projecting \vec{B} onto the direction perpendicular to neutral density surfaces, $\nabla b / |\nabla b|$, where ∇b is the adiabatic buoyancy gradient:

$$\kappa_{\text{eff}} = -\frac{\vec{B} \cdot \nabla b}{|\nabla b|^2}. \quad (14)$$

In the absence of an available online κ_{eff} code in our ALB solution, we make an offline estimation by computing the net \vec{B} from the diagnosed T and S mixing fluxes using the locally linearized EOS as in (12) and the adiabatic buoyancy gradient via the stiffened nonlinear EOS introduced above. The profile in Fig. 10 across the Mediterranean Sea shows bottom-intensified mixing near the bottom reaching above the BBL height by hundreds of meters, especially over the slopes, with magnitudes much larger than in the interior, as well as elevated values in the surface boundary layer. We plot $|\kappa_{\text{eff}}|$ because there are occasional small negative values of κ_{eff} due to the uncontrolled sign of model discretization errors. These distributions are at least qualitatively consistent with the abyssal mixing measurements (Waterhouse et al. 2014), from which interior values of $O(10^{-4}) \text{ m}^2 \text{s}^{-1}$ are estimated in the deep ocean, but increase to $O(10^{-2}) \text{ m}^2 \text{s}^{-1}$ near topography. Even if our model’s mixing might be quantitatively inaccurate, we do expect the simulated structure of the slope currents, buoyancy balance, and momentum balance (section 5) to be robust, partly

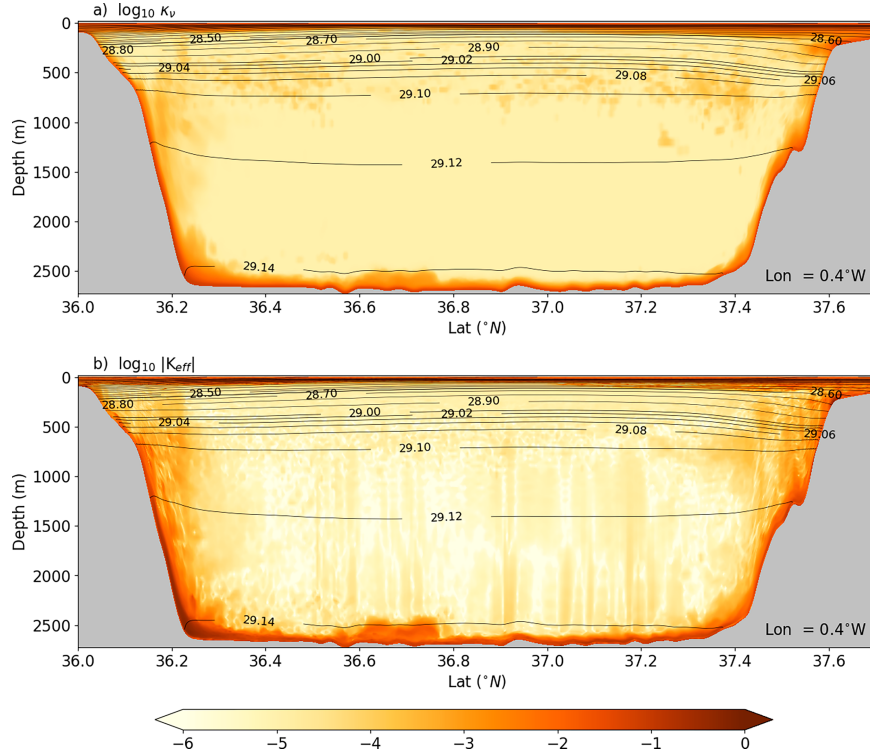


FIG. 10. The time-averaged eddy diffusivity $\kappa(y, z)$ ($\text{m}^2 \text{s}^{-1}$) in the ALB simulation along a section at 0.4°W , approximately between Oran and the coast near Cartagena (see Fig. 2b): (a) vertical κ_v as diagnosed with the KPP parameterization and (b) diapycnal κ_{eff} as diagnosed from the total diapycnal mixing (J. Gula et al. 2024, unpublished manuscript). The black lines are adiabatic density surfaces.

based on extensive studies of mixing sensitivity in 1D models (sections 7 and 8).

To show the typicality of the topographic regime, area-averaged profiles made over steep slopes in the whole of the abyssal Alboran Sea in the ALB simulation are shown in Fig. 11. These averages are conditioned on a minimum slope magnitude, $|\nabla h|$; as this minimum is decreased (from $\log_{10}|\nabla h| > -0.8$ to $\log_{10}|\nabla h| > -1.3$), the amplitudes of all the plotted quantities decrease, but the shapes remain nearly the same. (Because these are averages over many locations of quantities that are non-linearly related to each other, these averaged profiles should not be viewed as relevant to any particular place.) Topographic currents are the norm, reaching well above the BBL; downhill flow occurs adjacent to the slope; and diapycnal downwelling [$\tilde{\omega} > 0$ in (5)] occurs in the bulk of the boundary layer. The cross-isobath mean flow turns uphill above the boundary layer along with diapycnal upwelling. As mentioned above, the mean buoyancy balance again reverses sign in a thin layer very close to the slope. The prevalence of net diapycnal downwelling within the BBL is reflected by the cumulative integral of the mixing term shown in Fig. 11h, which is negative well into the nearby interior before turning positive above. Finally, the effective diffusivity profiles reflect bottom-intensified mixing reaching far above the BBL.

Figure 12a shows the decomposition of the advective tendency term, $-\bar{\mathbf{u}} \cdot \nabla b$, into the contributions of the time-mean

flow, $-\bar{\mathbf{u}} \cdot \nabla b$, and the eddies, $-\bar{\mathbf{u}}' \cdot \nabla b'$. It demonstrates that the contribution of the mean current (solid gray line) is always positive near the bottom, increasing the local buoyancy by advecting less dense water downhill, while the contribution of eddy advection (dashed gray line) is always negative. The net buoyancy advection is thus a competition between these two contributions. In the bulk of the boundary layer, the positive mean advection dominates. However, the negative eddy advection is the cause of the reversal of the mean buoyancy balance signs in the thin layer at the slope (Fig. 11e).

The source of this negative eddy buoyancy advection is indicated in Fig. 12b, which shows a vertically extensive profile of negative eddy buoyancy flux, $\bar{w}'b' < 0$, that is also the rate of conversion of eddy kinetic energy to eddy potential energy. This implicates mean flow shear instability as the source of eddy energy followed by the conversion to potential energy. Furthermore, because the principal gradients of the mean currents on the broader scale of the abyssal slopes are vertical (Figs. 11a,b), it seems likely that it is a vertical shear instability phenomenon, i.e., an ageostrophic process on a scale larger than boundary layer turbulence. The negative sign of $\bar{w}'b'$ is inconsistent with BBL baroclinic instability and thus is contrary to the circumstances analyzed in Callies (2018) and Drake et al. (2022).

The 1D profiles in Fig. 12 plotted versus H_{ab} show the area-averaged values for the Cartagena domain (solid) and

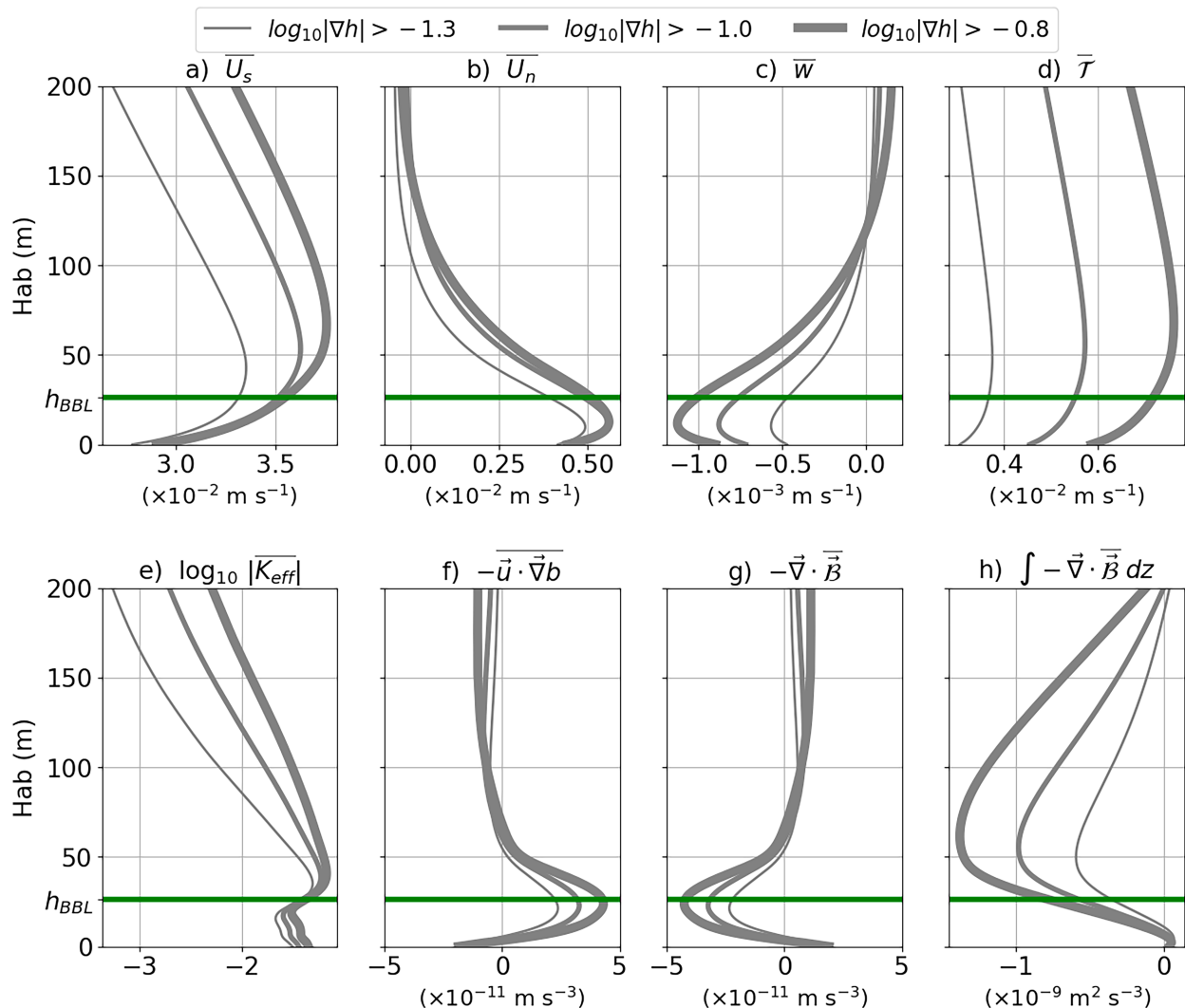


FIG. 11. Area- and time-averaged, near-bottom vertical profiles for (a) horizontal current in the along slope (topostrophic) direction, (b) horizontal current in the cross-slope direction, (c) \bar{w} , (d) $\bar{\tau}$, (e) $\log_{10}|\bar{K}_{eff}|$, (f) $-\bar{u} \cdot \bar{\nabla} b$, (g) $-\bar{\nabla} \cdot \bar{\mathcal{B}}$, and (h) the cumulative vertical integral of $-\bar{\nabla} \cdot \bar{\mathcal{B}}$, plotted against height above the bottom (Hab). The averaging area is the whole of the ALB domain east of Gibraltar Strait and with steep slopes, applying different minimum thresholds for the slope steepness, $\log_{10}|\nabla h|$ (as indicated by the line thicknesses). The green line is the mean BBL height.

for the whole Alboran Sea domain in regions with seafloor deeper than 800 m.

7. 1D topostrophy-mixing-slope BBL

To provide a framework for interpreting the flow structure and dynamical balances in the preceding sections, we redo the 1D BBL analysis following Garrett (1990) but insisting on a topostrophic interior flow and also including eddy buoyancy transport. The existence of the latter effects is demonstrated by the buoyancy and momentum analyses in sections 5 and 6, and they are due to dynamical processes that are not directly associated with the boundary layer turbulence.

The 1D model is for steady flow and buoyancy profiles adjacent to a uniform slope. In the interior, the solution asymptotes

to a uniform along-isobath horizontal velocity U_∞ with uniform stratification $b_\infty(z) = N^2 z$, both in geostrophic, hydrostatic balance with the geopotential field $\Phi_\infty(y, z) = -f U_\infty z + N^2 z^2/2$.¹

The model is expressed in rotated (X , Y , and Z) coordinates to align with the sloping bottom at $Z = 0$. The coordinate transformation is

¹ The background stratification is not necessarily a constant N if $\kappa(z)$ is variable. Rather than developing a more general background balance model, we implicitly assume a background right-side maintenance term in the buoyancy balance, $B_0(Z) = -\partial z(\kappa N^2)$, to cancel any N evolutionary tendency and to focus on the boundary layer dynamics. This is consistent with most previous 1D BBL analyses, and it might well implicate interior buoyancy ADV and circulation, as in Callies (2018) and Drake et al. (2022).

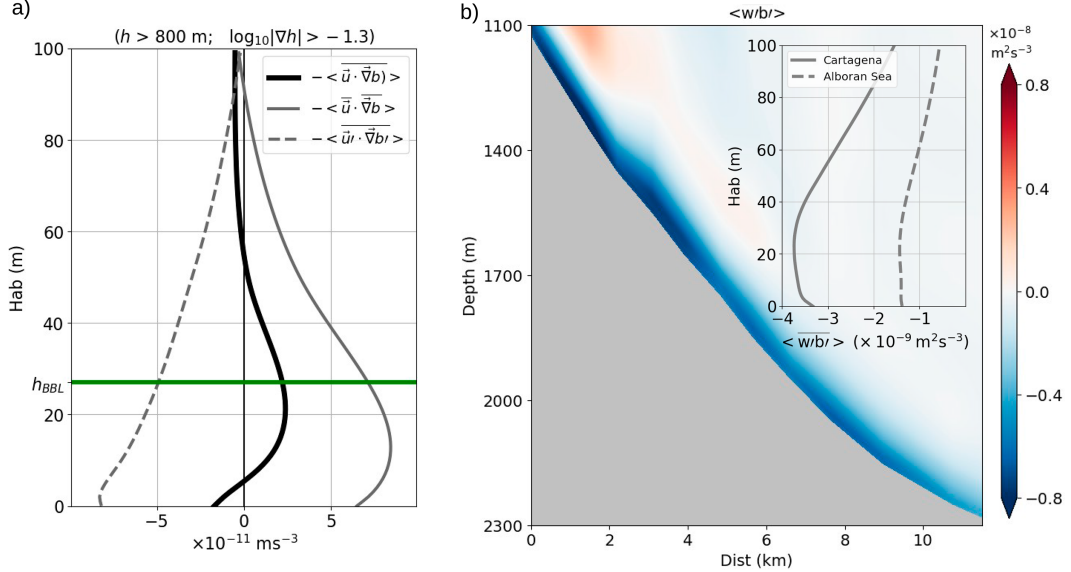


FIG. 12. (a) Area- and time-averaged near-bottom vertical profiles for $-\bar{u} \cdot \nabla b$ (as shown in Fig. 11 for $\log_{10}|\nabla h| > -1.3$; black), the corresponding input from the time-mean flow $\bar{u} \cdot \nabla b$ (solid gray), and the eddy contribution $-u' \cdot \nabla b'$ (dashed gray), plotted against height above the bottom Hab . The averaging area is the whole of the ALB domain, east of Gibraltar Strait, for $h \geq 800$ m. The green line is the mean BBL height. (b) Time-averaged and along-isobath-averaged cross sections on the Cartagena slope for the baroclinic term $\langle w' \cdot b' \rangle$, which entails a conversion from eddy available potential energy to EKE through baroclinic instabilities if the term is positive. The profiles in the inset box correspond to the area-averaged quantities plotted against Hab and for $h \geq 800$ m in the same region (Cartagena slope; solid) and for the whole ALB domain east of Gibraltar Strait (dashed).

$$X = x, Y = y \cos[\theta] + z \sin[\theta], Z = -y \sin[\theta] + z \cos[\theta], \quad (15)$$

where $\theta > 0$ is the angle of the sloping bottom upward to the north. In these coordinates,

$$\begin{aligned} b_\infty &= N^2(\sin[\theta]Y + \cos[\theta]Z), \\ \Phi_\infty &= -fU_\infty(\cos[\theta]Y - \sin[\theta]Z) + \frac{N^2}{2}(\sin[\theta]Y + \cos[\theta]Z)^2. \end{aligned} \quad (16)$$

The velocity $\mathbf{u} = (U, V, W)$ is similarly rotated into this slope-aligned coordinate system. For $f > 0$, a topographic flow has $U_\infty < 0$. Notice that this configuration matches the sketch in Fig. 1, i.e., $\hat{\mathbf{s}} = -\hat{\mathbf{X}}$ for $f > 0$.

The 1D BBL problem matches this interior solution (with only along-isobath flow, i.e., $V_\infty = W_\infty = 0$) with boundary conditions at the slope with a no-slip velocity, $\mathbf{u} = 0$, and no buoyancy flux, $\kappa \partial_Z b = 0$, at $Z = 0$ for general, slope-normal eddy viscosity and diffusivity profiles, $\nu(Z)$ and $\kappa(Z)$, respectively. It seeks solutions that depend only on Z apart from a uniform Y dependency in b such that $\partial_Y b = N^2 \sin[\theta]$, a constant, the same as for $\partial_Y b_\infty$. Thus, the ordinary differential equation (ODE) system for deviations from the interior fields (denoted by $b' = b - b_\infty$, etc.) is

$$-f \cos[\theta]V' = \partial_Z(\nu \partial_Z U') + F',$$

$$f \cos[\theta]U' = \sin[\theta]b' + \partial_Z(\nu \partial_Z V'),$$

$$f \sin[\theta]U' = -\partial_Z \Phi' + \cos[\theta]b',$$

$$N^2 \sin[\theta]V' = \partial_Z(\kappa \partial_Z b') + B'_e. \quad (17)$$

The boundary conditions are

$$\begin{aligned} U' &= -U_\infty, V' = 0, \kappa \partial_Z b' = -N^2 \kappa \cos[\theta] \quad \text{at } Z = 0, \\ U', V', b' &\rightarrow 0 \quad \text{as } Z \rightarrow \infty. \end{aligned} \quad (18)$$

These equations are linear in the dependent variables; the only advective term retained is the cross-isobath buoyancy advection, i.e., V' times the constant $\partial_Y b$. The $W' = 0$ everywhere. This system has forcing terms proportional to $F'(Z)$ and $B'_e(Z)$ in the interior of the ODE system and U_∞ and $N^2 \cos[\theta]$ in the boundary conditions, but not all of these are independent as explained below.

The $F'(Z)$ is the boundary layer deviation from the ADV + PGF + COR = 0 interior balance in the along-isobath mean momentum balance (section 5). It represents the ADV' + PGF' terms associated with the eddy advection or other process that causes topography but is otherwise absent from (17); its role is to convey this effect into the BBL dynamics. The $B'_e(Z)$ represents the eddy buoyancy advection, $-\langle u' \cdot \nabla b' \rangle$ in Fig. 12a, also otherwise absent in (17). Both F' and $B'_e \rightarrow 0$ as $Z \rightarrow \infty$.

[Garrett \(1990\)](#) shows how to solve this system when $F' = B'_e = 0$, partly by recasting it in terms of the cross-isobath streamfunction $\psi'(Z)$ with $V' = \partial_Z \psi'$. By elimination of other variables, the ODE system for ψ' in a domain $[0, Z_{\max}]$ is as follows:

$$\begin{aligned} \partial_Z^2(\nu \partial_z^2 \psi') + 4\nu q^4 \psi' &= 4\nu q^4 \left(\kappa_0 \operatorname{ctn}[\theta] + \frac{1}{N^2 \sin[\theta]} \int_0^\infty B'_e dZ \right) \\ &\quad + \frac{f \cos[\theta]}{\nu} \int_Z^\infty F' dZ - \frac{\sin[\theta]}{\kappa} \int_Z^\infty B'_e dZ, \\ \psi' &= \partial_Z \psi' = 0 \quad \text{at } Z = 0, \\ \psi' &\rightarrow \kappa_0 \operatorname{ctn}[\theta] + \frac{1}{N^2 \sin[\theta]} \int_Z^\infty B'_e dZ, \quad \partial_Z \psi' \rightarrow 0 \quad \text{as } Z_{\max} \rightarrow \infty, \end{aligned} \quad (19)$$

where $\kappa_0 = \kappa(0)$ and

$$q^4 = \frac{1}{4} \left(\frac{f^2 \cos^2[\theta]}{\nu^2} + \frac{N^2 \sin^2[\theta]}{\nu \kappa} \right). \quad (20)$$

Given a solution for $\psi'(Z)$, we can evaluate the other profiles by

$$\begin{aligned} b'(Z) &= -N^2 \sin[\theta] \int_Z^\infty \left[(\psi' - \kappa_0 \operatorname{ctn}[\theta]) \right. \\ &\quad \left. - \frac{1}{N^2 \sin[\theta]} \int_0^\infty B'_e dZ'' \right] \frac{dZ'}{\kappa(Z')} - \int_Z^\infty B'_e dZ'' \frac{dZ'}{\kappa(Z')}, \\ U'(Z) &= \frac{f \cos[\theta]}{\nu} \int_Z^\infty \left[(\psi' - \kappa_0 \operatorname{ctn}[\theta]) \right. \\ &\quad \left. - \frac{1}{N^2 \sin[\theta]} \int_0^\infty B'_e dZ'' \right] \frac{dZ'}{\nu(Z')} - \int_Z^\infty \left(\int_Z^\infty F' dZ'' \right) \frac{dZ'}{\nu(Z')}, \\ V'(Z) &= \partial_Z \psi', \end{aligned} \quad (21)$$

together with the bottom stress, $\tau = \nu \partial_Z(U', V')(0)$, and lateral transport anomaly, $T' = \int_0^\infty (U', V') dZ$. Notice that U_∞ does not appear explicitly in (19)–(21); thus, the only forcing terms are $\kappa_0 \operatorname{ctn}[\theta]$, F' , and B'_e , while $U_\infty = -U'(0)$ is implicit.

Our purpose with this model is as a paradigm for explaining the topographic boundary layer structure evident in the ROMS simulations, rather than as a deliberate fit at any particular location. In this spirit, we choose simple boundary layer profile shapes for the forcing functions, e.g.,

$$F'(Z) = F_0 e^{-\ell Z}, \quad B'_e(Z) = B_{e0} e^{-\mu Z}, \quad (22)$$

and “typical” values for the parameters to illustrate the solution behavior. With both analytic solutions ([appendix](#)) and a numerical solver for (19)–(21), we have extensively explored different parameter values and different profile shapes for ν , κ , F' , and B'_e . While these choices have meaningful quantitative consequences for the 1D solutions, their qualitative shapes are quite robust for positive diffusivities and mostly negative values for F' and B'_e , consistent with the near-boundary mixing, momentum advection, and eddy buoyancy advection shown in [sections 5](#) and [6](#). Therefore, we restrict our attention

here to a representative set of solutions with constant ν and κ ; this choice of parameter values is not delicate with respect to demonstrating the relevant behaviors. In our view, the value of the 1D model is as an idealized demonstration of the influence of topostrophy on the slope BBL—and as making a connection with the conventional 1D model of [Garrett \(1990\)](#)—rather than as a quantitative explanation of the simulation results.

The solution procedure is to decompose the solution into superimposable pieces:

$$\psi' = \psi'_{\kappa_0, B''} + \psi'_F, \quad (23)$$

etc., where $\psi'_{\kappa_0, B''}$ satisfies the boundary value problem (BVP) (19) for $F' = 0$ and ψ'_F satisfies the BVP (19) for all the terms with κ_0 and B'_e set to zero and $F' \neq 0$. The latter is initially specified with an arbitrary multiplicative coefficient that is then renormalized such that

$$U'_F(0) = -[U_\infty + U'_{\kappa_0, B'}(0)], \quad (24)$$

where U_∞ is specified. This renormalization factor is applied to all the \cdot_F functions. The total solution is then evaluated by summation as in (23).

The 1D BBL solutions with representative parameter values are in [Fig. 13](#) for three cases: 1) a mixing BBL where $F' = B'_e = 0$ and

$$U'_{\kappa_0} = \frac{f \kappa \cos[\theta] \operatorname{ctn}[\theta]}{\nu q} > 0 \quad (25)$$

is fully determined and directed opposite to topographic interior flow (cf. [Garrett 1990](#)); 2) a topographic BBL with momentum advection where $B'_e = 0$ and U_∞ has the specified value by the choice of F_0 ; and 3) a topographic BBL with both momentum advection and eddy buoyancy advection where both F' and B'_e are nonzero.

[Figure 13](#) shows the primary profiles for the three cases. As a broad summary statement, the topographic boundary layers are very different from the mixing boundary layer. The $b'(z)$ is positive in all cases as a reflection of the requirement for the interior stratification to transition to a no-buoyancy-flux boundary condition. The along-isobath flow $U(z)$ monotonically increases from its no-slip zero value at the slope and has the opposite sign, by construction when $F' \neq 0$, due to the requirement that it matches with the topographic interior value ($U_\infty < 0$ such that $\bar{T} > 0$). The cross-isobath flow $V'(Z)$ is also in the opposite direction near the boundary with topostrophy, i.e., it is downhill there, consistent with $w_b < 0$. In all cases, V' reverses sign with distance above the boundary; its net lateral transport $T'' = \psi'(\infty)$ is positive in the 1) mixing and 2) only topographic cases but becomes net negative in case 3 with $B'_e \neq 0$. These topographic BBL solutions in cases 2 or 3 are the basis for the sketch in [Fig. 1](#).

As U_∞ becomes more negative (i.e., more topographic), the strength of the near-boundary downhill flow in V' increases, e.g., for the parameters otherwise as in [Fig. 13](#) for case 2, this $V' < 0$ regime occurs for all $U_\infty < -0.02 \text{ m s}^{-1}$. As B_{e0}

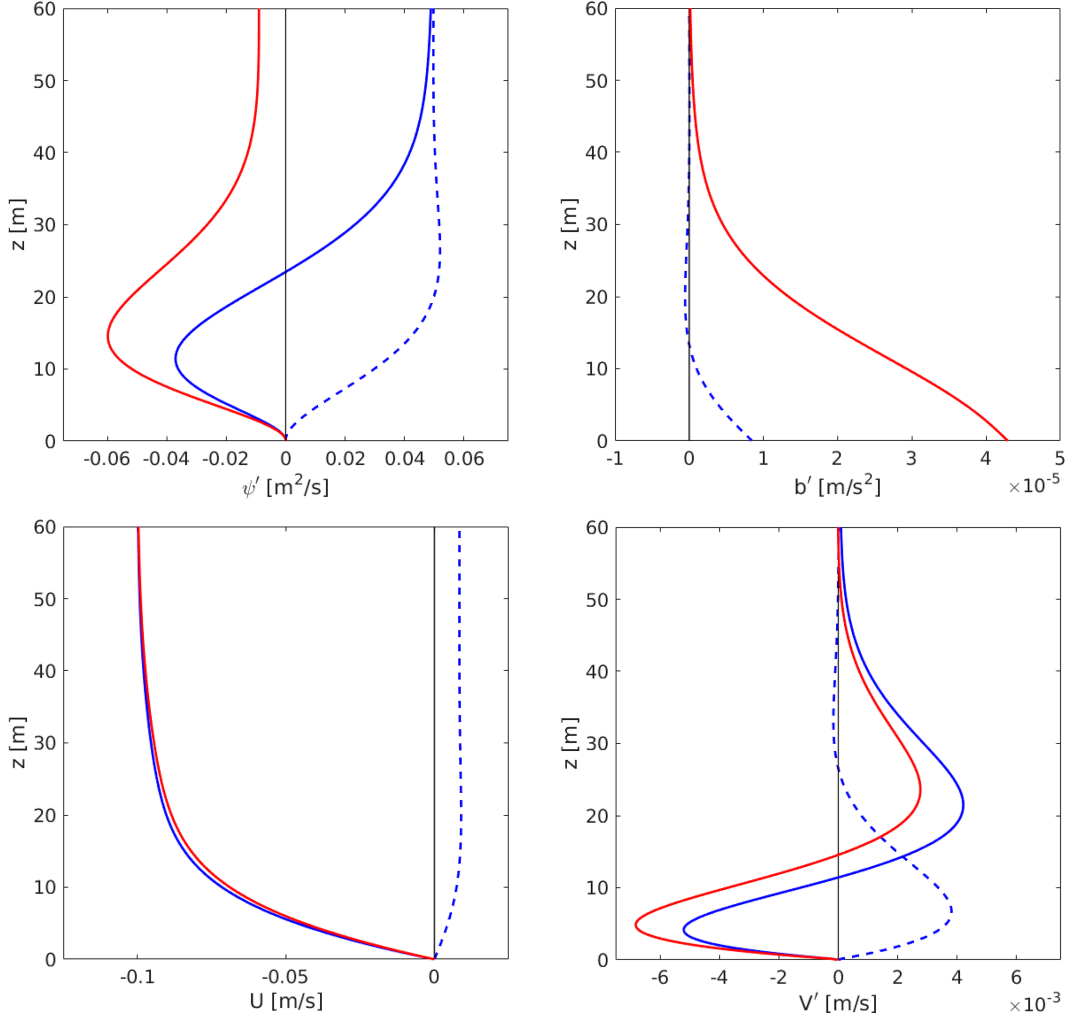


FIG. 13. Vertical profiles in the 1D BBL with constant diffusivities: from upper left clockwise, cross-hill streamfunction ψ' , buoyancy anomaly b' , total along-isobath flow U , and uphill flow V' . The blue dashed lines are for the mixing BBL ($F' = B'_e = 0$); the blue solid lines are for topostrophic BBL with momentum ADV ($F' \neq 0, B'_e = 0$); and the red solid lines are for the topostrophic BBL with both momentum ADV and eddy buoyancy ADV ($F', B'_e \neq 0$). For b' , the blue and red solid curves nearly coincide, and for U , they are also close. When $F' \neq 0$, $\ell = 0.09 \text{ m}^{-1}$ and $F_0 = -5.82 \times 10^{-6}$ or $-4.92 \times 10^{-6} \text{ m s}^{-2}$ for the cases without or with $B_{e0} \neq 0$, respectively, to assure the value of $U_\infty = -0.1 \text{ m s}^{-1}$. When $B'_e \neq 0$, $\mu = 0.05 \text{ m}^{-1}$ and $B_{e0} = -3 \times 10^{10}$. Other parameters are $f = 10^{-4} \text{ s}^{-1}$, $\kappa = \nu = 0.5 \times 10^{-2} \text{ m}^2 \text{s}^{-1}$, $\theta = 0.1$, $N^2 = 10^{-6} \text{ s}^{-2}$, and $q = 0.12 \text{ m}^{-1}$.

becomes more negative, the cross-slope transport T'' becomes more downhill; e.g., for the parameters otherwise as in Fig. 13 for case 3, the marginal value for this regime is $B_{e0} = -2.5 \times 10^{-10} \text{ m s}^{-3}$. That is, the essential behaviors of downhill flow, $V'(0) < 0$, and near-slope diapycnal downwelling are robust across wide variations in the 1D model with topostrophy, while the value and sign of the total cross-slope transport, $\psi'(\infty) = T''$, are more variable depending on the relative importance of B'_e .

The signs of these near-slope $V'(Z)$ are consistent with Ekman layer thinking in the sense that they are directed to the left of the along-isobath interior flows U_∞ . However, the sign reversals in $V'(Z)$ are inconsistent with the relation between lateral Ekman transport \mathbf{T}' and the bottom stress τ [both

defined following (21)]. In none of these three cases are either of the lateral Ekman transport relations satisfied. In particular, after vertically integrating the X -momentum equation in (17) and using the $\partial_Z U'(0)$ boundary condition in (18), the cross-isobath transport relation is

$$T'' - \frac{\tau'}{f \cos[\theta]} = -\frac{1}{f \cos[\theta]} \int_0^\infty F' dz, \quad (26)$$

and the nonzero right-side momentum advection breaks the Ekman relation. (The along-isobath transport relation has a more complicated formula, not shown here.) In the limit of a flat bottom ($\theta \rightarrow 0$) and no topostrophic or eddy buoyancy advection forcing ($F' = B'_e = 0$), these relations revert to Ekman layer transport.

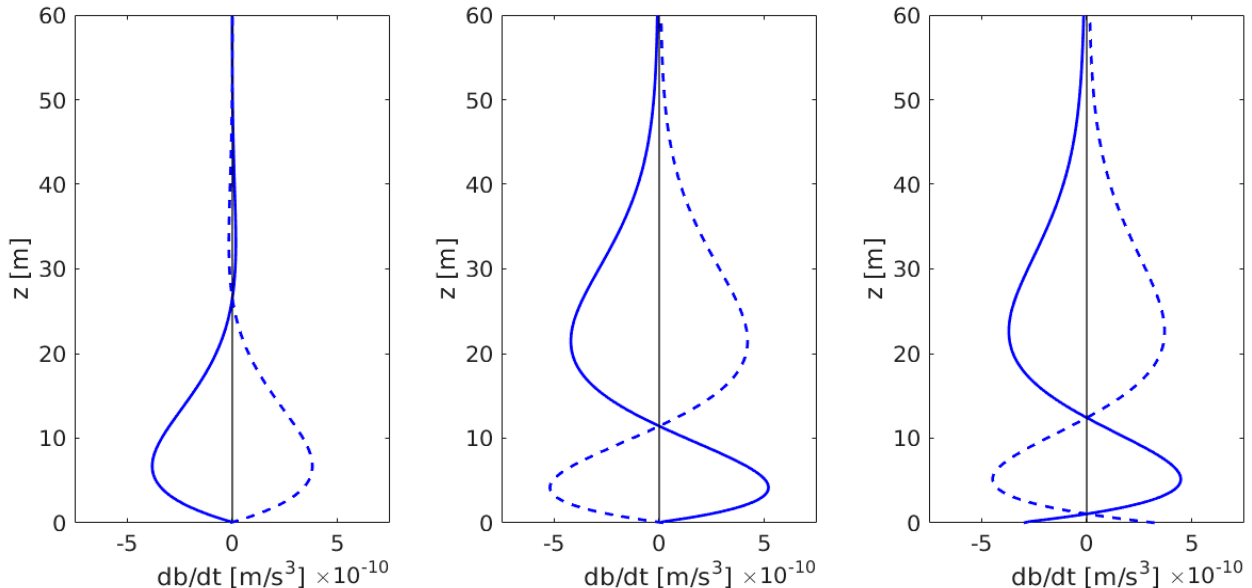


FIG. 14. The 1D BBL buoyancy balance terms: mean plus eddy ADV (solid) and slope-normal diffusion (dashed). Shown from left to right, the cases are the mixing BBL ($F' = B'_e = 0$), the topographic BBL with momentum ADV ($F' \neq 0, B'_e = 0$), and the topographic BBL with both momentum ADV and eddy buoyancy ADV ($F', B'_e \neq 0$). The parameters are the same as in Fig. 13.

The eddy buoyancy advection B'_e has a moderate quantitative influence on the topographic BBL profiles, slightly so for b' and U and more so for ψ' and V' , but not a qualitatively large one (Fig. 13), except perhaps for the sign of T''^y that is determined by a competition between buoyancy mixing and eddy advection. Where the role of B'_e becomes evident is in comparing cases 2 and 3 for their mean buoyancy balance in (17) (Fig. 14) between net buoyancy advection, $-N^2 \sin[\theta] V' + B'_e$, and turbulent buoyancy mixing, $\partial_Z(\kappa \partial_Z b')$. In mixing-only case 1, advection tends to decrease the buoyancy as an upslope advection, while mixing tends to increase it (i.e., diapycnal upwelling). In contrast, in topographic cases 2 and 3, the lower part of the boundary layer has an advective buoyancy increase and diapycnal downwelling. However, in a very thin layer near the slope, case 3 shows a small amount of diapycnal upwelling due to $B'_e \neq 0$ (cf. Fig. 11e).

The 1D topographic BBL model is therefore a useful paradigm for abyssal slope currents. Here, we have only shown representative solutions. The parameter values and profile shapes for κ , ν , F' , and B'_e could be varied to explore their sensitivities, but it seems to us much more important to look to further measurements and simulation models like ours to better determine what the true distributions are for diapycnal mixing, topographic momentum mixing, and eddy buoyancy fluxes near the abyssal slopes.

The mixing-only 1D BBL model has been very influential in ideas about abyssal upwelling near slopes (section 1), and the widespread prevalence of topostrophy is an important corrective to such arguments, as further discussed in section 8. Topostrophy is also an important correction to the “arrested Ekman layer” idea that initial interior flows on slopes evolve toward the mixing-only steady state with a weak U_∞ (e.g., Garrett et al. 1993; Brink and Lentz 2010; Ruan et al. 2019,

2021) when there are no confounding interior dynamics to counter this evolution. In 3D flows with sustained interior flows, the tendency toward arrest is weaker (Jagannathan et al. 2023), in particular in topographic situations.

We can contrast this 1D steady, stratified, slope BBL model with the conventional 1D steady Ekman layer model for unstratified flow above a flat bottom, both with constant eddy mixing coefficients. The connection between these simple models is not direct, i.e., in the limit of $\theta \rightarrow 0$ with other parameters held constant; the former has $(U_{\infty}, V') \rightarrow \infty$ because (17) and (18) imply nonzero stratification and lateral buoyancy advection (see appendix formulas). In other words, the conventional Ekman BBL model does not encompass stratification, which is an essential part of the slope BBL models. To properly span these two regimes, a more general BBL model is required.

8. Discussion

This is an era of increasing appreciation of the dynamical importance of the ocean’s abyssal topographic slopes: boundary layer turbulence, inertia–gravity wave and vorticity generation, adjacent interior diapycnal mixing due to breaking waves and wakes, along-isobath (topostrophic) flows, and eddy fluxes.

The primary contributions in this paper are demonstrating widespread topostrophy and how this feature and momentum and buoyancy advection and turbulent mixing in the near-slope region lead to a down-slope mean flow and extensive diapycnal downwelling, taking a coarse-grained view beyond small-scale canyons and ridges. A similar result is reported in Schubert et al. (2024, manuscript submitted to *Nat. Geosci.*) for an analogous simulation in the Atlantic Ocean. Relative

to the scientific literature, in our view, this amplifies the importance of eddy-driven topostrophy, and it provides an important modification to the recent advocacy of slope-adjacent diapycnal upwelling (Ferrari et al. 2016; de Lavergne et al. 2016; McDougall and Ferrari 2017; Callies and Ferrari 2018; de Lavergne et al. 2016; Holmes et al. 2018, 2019; Drake et al. 2020; Holmes and McDougall 2020; Drake et al. 2022; Peterson and Callies 2022; Baker et al. 2023; Peterson and Callies 2023; Wynne-Cattanach et al. 2024).

A strong rationale for the slope-upwelling view has been the 1D slope BBL model (e.g., Garrett 1990) and its elaborations with various depictions of the vertical profile of bottom-enhanced mixing. We show how this is modified by a topostrophic flow in section 7 to reverse the slope-adjacent flow but still have diapycnal upwelling in the outer part of the BBL and nearby interior. The global thermohaline circulation requires net diabatic and volumetric upwelling in the abyss, of course, and because of the locally enhanced diabatic mixing, it seems likely that much if not most of it occurs in topographic neighborhoods. However, regional models, such as the ones analyzed here and in Schubert et al. (2024, manuscript submitted to *Nat. Geosci.*), are not the right tool for assessing the net global upwelling because they are strongly influenced by imposed abyssal inflows through their open lateral boundaries.

9. Summary and prospects

Abyssal slope currents are significantly topostrophic, due, in a general way, to turbulent “mesoscale” oceanic momentum dynamics. This phenomenon leads to both downhill mean flow and diapycnal slope downwelling, as well as nearby upwelling. These are widespread phenomena sustained by boundary layer turbulence and adjacent diapycnal mixing.

This paper and its companion (Schubert et al. 2024, manuscript submitted to *Nat. Geosci.*) comprise a synthesis and partial revision of several prevailing ideas about oceanic circulation and mixing: geostrophic topographic turbulence, slope bottom boundary layers, near-slope mean flow eddy instability, and abyssal upwelling due to bottom-intensified diapycnal mixing. However, current-topography interaction in the abyss remains a significant scientific frontier. Apart from simple idealized configurations, it involves demanding computational simulation capabilities for mesoscale eddies, the bottom kinematic boundary condition, bottom boundary layer turbulence, topographic vertical vorticity and inertia-gravity wave generation, and submesoscale wakes—all in their appropriate context for a realistic regional circulation.

In our view, further progress lies ahead via improved model formulations and finer grid resolutions in both idealized and realistic configurations. Further investigations are needed for three particular issues in abyssal slope regions: 1) the spatial distribution of diapycnal mixing in the mean buoyancy balance, 2) the advective “eddy driving” for topostrophic mean flow and the dynamical conditions under which it is a dominant effect, and 3) local currents in canyons and ridges

that underlie the generally topostrophic slope flow, including tidal effects.

Acknowledgments. The authors acknowledge helpful discussions with Andrew Stewart. Support for this research was provided by the Office of Naval Research (ONR Grants N00014-18-1-2599 P00001 and N00014-23-1-2226) and the National Science Foundation (NSF Grant 2241754). J.G. and R.S. gratefully acknowledge support from the French National Agency for Research (ANR) through the project DEEPER (ANR-19-CE01-0002-01). Computing support was provided by the NSF ACCESS program.

Data availability statement. The ALB model simulation used in this work was performed using the UCLA version of the ROMS model (<https://github.org/CESR-lab/ucla-roms.git>). Configuration files and an output sample are available at <https://doi.org/10.5281/zenodo.10215065> (Capó 2023).

APPENDIX

1D BBL Relations

Here, we present 1D BBL solutions in analytic form. For brevity, we do not include cases with $\mathbf{B}' \neq 0$. The problem is posed in section 7, and representative solutions are in Fig. 13. Because of the linearity of (19), we can superimpose the separate solutions for each forcing, e.g.,

$$U' = U'_\kappa + U'_F, \quad (\text{A1})$$

where U'_κ is the solution with $F' = 0$ and U'_F is the solution with a homogeneous buoyancy boundary condition, $\partial_Z b' = 0$. We designate them as the buoyancy mixing and topostrophic components, respectively. For each of these, U_∞ is fully determined. For U'_F , we will take the inverse view that $F'(Z)$ is chosen such that U_∞ has the desired topographic value.

The solutions specified below are plotted in Fig. 13 for the parameter values listed in the caption.

a. Mixing BBL

First, consider the case with $F' = 0$ [referred to as case 1 in section 7]. Its solution with constant ν and κ is presented in Garrett (1990). The formula is

$$\psi'_\kappa(Z) = \kappa \operatorname{ctn}[\theta] [1 - e^{-qz} (\sin[qz] + \cos[qz])]. \quad (\text{A2})$$

The other profiles are

$$b'_\kappa(Z) = \frac{N^2 \cos[\theta]}{q} e^{-qz} \cos[qz],$$

$$U'_\kappa(Z) = -U_* e^{-qz} \cos[qz],$$

$$V'_\kappa(Z) = 2\kappa \operatorname{ctn}[\theta] e^{-qz} \sin[qz], \quad (\text{A3})$$

where the surface value of the along-isobath velocity anomaly is $U'_\kappa(0) = -U_*$ with

$$U_* = \frac{f\kappa \cos[\theta] \operatorname{ctn}[\theta]}{\nu q} > 0. \quad (\text{A4})$$

As anticipated, this solution is consistent only with a retrograde interior along-isobath velocity, i.e., the opposite of topostrophy.

b. Topostrophic BBL

Now consider the solution with $F' \neq 0$ with no terms explicitly proportional to κ in (19)–(21) because they are accounted for in the mixing BBL solution but still with a κ dependency in both q and the denominator of the coefficient for $b'(Z)$. For the 1D BBL problem, F' is not known a priori because it is considered to be a product of the 3D interior topostrophic dynamics. This product is conveyed into the BBL problem by requiring that the total $U(Z) \rightarrow U_\infty$ as $Z \rightarrow \infty$ with a specified U_∞ value. For the U'_F surface boundary condition from (18), this implies that

$$U'_F(0) = -(U_\infty - U_*). \quad (\text{A5})$$

Then, $F'(Z)$ is chosen such that this condition is satisfied. Thus, we can specify a simple representative shape

$$F'(Z) = F_0 e^{-\ell Z}, \quad (\text{A6})$$

whose amplitude F_0 is chosen to satisfy (A5). The analytic solution for $\ell \neq q$ is

$$\begin{aligned} \psi'_F(Z) &= \psi_0 \left[e^{-\ell Z} - \cos[qZ] e^{-qZ} + \left(\frac{\ell}{q} - 1 \right) \sin[qZ] e^{-qZ} \right], \\ b'_F(Z) &= -\frac{N^2 \sin[\theta] \psi_0}{\ell \kappa} \left[e^{-\ell Z} - \frac{\ell}{q} \cos[qZ] e^{-qZ} + \frac{\ell^2}{2q^2} (\sin[qZ] \right. \\ &\quad \left. + \cos[qZ]) e^{-qZ} \right], \\ U'_F(Z) &= \left(\frac{f \cos[\theta] \psi_0}{\ell \nu} - \frac{F_0}{\ell^2 \nu} \right) e^{-\ell Z} - \frac{f \cos[\theta] \psi_0}{q \nu} \cos[qZ] e^{-qZ} \\ &\quad + \frac{f \ell \cos[\theta] \psi_0}{2q^2 \nu} (\sin[qZ] + \cos[qZ]) e^{-qZ}, \\ V'_F(Z) &= \psi_0 [-\ell e^{-\ell Z} + 2q \sin[qZ] e^{-qZ} + \ell(\cos[qZ] \\ &\quad - \sin[qZ]) e^{-qZ}], \end{aligned} \quad (\text{A7})$$

where

$$\begin{aligned} \psi_0 &= \frac{f \cos[\theta]}{\ell \nu^2 (\ell^4 + 4q^4)} F_0 \quad \text{and} \\ F_0 &= (U_\infty - U_*) \left\{ \left(\frac{1}{\ell^2 \nu} - \frac{f^2 \cos^2[\theta]}{\ell^2 \nu^3} \left[\frac{1 - \ell/q + \ell^2/(2q^2)}{\ell^4 + 4q^4} \right] \right) \right\}. \end{aligned} \quad (\text{A8})$$

With the parameter values listed in the caption of Fig. 13, $F_0 = -5.8 \times 10^{-6} \text{ m s}^{-2}$, and $\psi_0 = -0.80 \text{ m}^2 \text{ s}^{-1}$ for the case referred to as case 2 in section 7.

REFERENCES

- Allen, J. T., D. A. Smeed, J. Tintoré, and S. Ruiz, 2001: Mesoscale subduction at the Almeria–Oran front: Part 1: Ageostrophic flow. *J. Mar. Syst.*, **30**, 263–285, [https://doi.org/10.1016/S0924-7963\(01\)00062-8](https://doi.org/10.1016/S0924-7963(01)00062-8).
- Alvarez, A., J. Tintoré, G. Holloway, M. Eby, and J. M. Beckers, 1994: Effect of topographic stress on circulation in the western Mediterranean. *J. Geophys. Res.*, **99**, 16053–16064, <https://doi.org/10.1029/94JC00811>.
- Baker, L. E., A. Mashayek, and A. C. Naveira Garabato, 2023: Boundary upwelling of Antarctic Bottom Water by topographic turbulence. *AGU Adv.*, **4**, e2022AV000858, <https://doi.org/10.1029/2022AV000858>.
- Becker, J. J., and Coauthors, 2009: Global bathymetry and elevation data at 30 arc seconds resolution: SRTM30_PLUS. *Mar. Geod.*, **32**, 355–371, <https://doi.org/10.1080/01490410903297766>.
- Bretherton, F. P., and D. B. Haidvogel, 1976: Two-dimensional turbulence above topography. *J. Fluid Mech.*, **78**, 129–154, <https://doi.org/10.1017/S002211207600236X>.
- Brink, K. H., and S. J. Lentz, 2010: Buoyancy arrest and bottom Ekman transport. Part I: Steady flow. *J. Phys. Oceanogr.*, **40**, 621–635, <https://doi.org/10.1175/2009JPO4266.1>.
- Callies, J., 2018: Restrification of abyssal mixing layers by submesoscale baroclinic eddies. *J. Phys. Oceanogr.*, **48**, 1995–2010, <https://doi.org/10.1175/JPO-D-18-0082.1>.
- , and R. Ferrari, 2018: Dynamics of an abyssal circulation driven by bottom-intensified mixing on slope. *J. Phys. Oceanogr.*, **48**, 1257–1282, <https://doi.org/10.1175/JPO-D-17-0125.1>.
- Capó, E., 2020: Submesoscale dynamics in the western Mediterranean Sea. Ph.D. dissertation, University of the Balearic Islands, 154 pp., <http://hdl.handle.net/11201/151819>.
- , 2023: ALB500_UCLA-ROMS simulation [dataset]. Zenodo, accessed 30 November 2023, <https://doi.org/10.5281/zenodo.10215065>.
- , and J. C. McWilliams, 2022: Coherent Lagrangian pathways near an East Alboran front. *J. Geophys. Res. Oceans*, **127**, e2021JC018022, <https://doi.org/10.1029/2021JC018022>.
- , —, E. Mason, and A. Orfila, 2021: Intermittent frontogenesis in the Alboran Sea. *J. Phys. Oceanogr.*, **51**, 1417–1439, <https://doi.org/10.1175/JPO-D-20-0277.1>.
- , —, and A. Jagannathan, 2023: Flow-Topography interaction along the Spanish slope in the Alboran Sea: Vorticity generation and connection to interior fronts. *J. Geophys. Res. Oceans*, **128**, e2022JC019480, <https://doi.org/10.1029/2022jc019480>.
- Chen, R., J. C. McWilliams, and L. Renault, 2021: Momentum governors of California undercurrent transport. *J. Phys. Oceanogr.*, **51**, 2915–2932, <https://doi.org/10.1175/JPO-D-20-0234.1>.
- de Lavergne, C., G. Madec, J. Le Sommer, A. J. G. Nurser, and A. C. Naveira Garabato, 2016: The impact of a variable mixing efficiency on the abyssal overturning. *J. Phys. Oceanogr.*, **46**, 663–681, <https://doi.org/10.1175/JPO-D-14-0259.1>.
- Drake, H. F., R. Ferrari, and J. Callies, 2020: Abyssal circulation driven by near-boundary mixing: Water mass transformations and interior stratification. *J. Phys. Oceanogr.*, **50**, 2203–2226, <https://doi.org/10.1175/JPO-D-19-0313.1>.
- , X. Ruan, J. Callies, K. Ogden, A. M. Thurnherr, and R. Ferrari, 2022: Dynamics of eddying abyssal mixing layers over sloping rough topography. *J. Phys. Oceanogr.*, **52**, 3199–3219, <https://doi.org/10.1175/JPO-D-22-0009.1>.
- Ferrari, R., A. Mashayek, T. J. McDougall, M. Nikurashin, and J.-M. Campin, 2016: Turning ocean mixing upside down. *J.*

- Phys. Oceanogr.*, **46**, 2239–2261, <https://doi.org/10.1175/JPO-D-15-0244.1>.
- Flexas, M. M., D. Gomis, S. Ruiz, A. Pascual, and P. León, 2006: *In situ* and satellite observations of the eastward migration of the Western Alboran Sea Gyre. *Prog. Oceanogr.*, **70**, 486–509, <https://doi.org/10.1016/j.pocean.2006.03.017>.
- Garrett, C., 1990: The role of secondary circulation in boundary mixing. *J. Geophys. Res.*, **95**, 3181–3188, <https://doi.org/10.1029/JC095iC03p03181>.
- , P. MacCready, and P. Rhines, 1993: Boundary mixing and arrested Ekman layers: Rotating stratified flow near a sloping boundary. *Annu. Rev. Fluid Mech.*, **25**, 291–323, <https://doi.org/10.1146/annurev.fl.25.010193.001451>.
- Herring, J. R., 1977: On the statistical theory of two-dimensional topographic turbulence. *J. Atmos. Sci.*, **34**, 1731–1750, [https://doi.org/10.1175/1520-0469\(1977\)034<1731:OTSTOT>2.0.CO;2](https://doi.org/10.1175/1520-0469(1977)034<1731:OTSTOT>2.0.CO;2).
- Hersbach, H., and Coauthors, 2020: The ERA5 global reanalysis. *Quart. J. Roy. Meteor. Soc.*, **146**, 1999–2049, <https://doi.org/10.1002/qj.3803>.
- Holloway, G., 1987: Systematic forcing of large-scale geophysical flows by eddy-topography interaction. *J. Fluid Mech.*, **184**, 463–476, <https://doi.org/10.1017/S0022112087002970>.
- , 1996: Neptune effect: Statistical mechanical forcing of ocean circulation. *Stochastic Modelling in Physical Oceanography*, R. J. Adler, P. Muller, and B. L. Rozovski, Eds., Birkhäuser, 207–219.
- , 2008: Observing global ocean topostrophy. *J. Geophys. Res.*, **113**, C07054, <https://doi.org/10.1029/2007JC004635>.
- Holmes, R. M., and T. J. McDougall, 2020: Diapycnal transport near a sloping bottom boundary. *J. Phys. Oceanogr.*, **50**, 3253–3266, <https://doi.org/10.1175/JPO-D-20-0066.1>.
- , C. de Lavergne, and T. J. McDougall, 2018: Ridges, seamounts, troughs, and bowls: Topographic control of the dia-neutral circulation in the abyssal ocean. *J. Phys. Oceanogr.*, **48**, 861–882, <https://doi.org/10.1175/JPO-D-17-0141.1>.
- , —, and —, 2019: Tracer transport within abyssal mixing layers. *J. Phys. Oceanogr.*, **49**, 2669–2695, <https://doi.org/10.1175/JPO-D-19-0006.1>.
- Jackett, D. R., and T. J. McDougall, 1995: Minimal adjustment of hydrographic profiles to achieve static stability. *J. Atmos. Oceanic Technol.*, **12**, 381–389, [https://doi.org/10.1175/1520-0426\(1995\)012<0381:MAOHPT>2.0.CO;2](https://doi.org/10.1175/1520-0426(1995)012<0381:MAOHPT>2.0.CO;2).
- Jagannathan, A., K. Srinivasan, J. C. McWilliams, J. Molemaker, and A. L. Stewart, 2023: Evolution of bottom boundary layers on three dimensional topography—Buoyancy adjustment and instabilities. *J. Geophys. Res. Oceans*, **128**, e2023JC019705, <https://doi.org/10.1029/2023JC019705>.
- Klinck, J. M., 1996: Circulation near submarine canyons: A modeling study. *J. Geophys. Res.*, **101**, 1211–1223, <https://doi.org/10.1029/95JC02901>.
- Large, W. G., J. C. McWilliams, and S. C. Doney, 1994: Oceanic vertical mixing: A review and a model with a nonlocal boundary layer parameterization. *Rev. Geophys.*, **32**, 363–403, <https://doi.org/10.1029/94RG01872>.
- Legg, S., 2021: Mixing by oceanic lee waves. *Annu. Rev. Fluid Mech.*, **53**, 173–201, <https://doi.org/10.1146/annurev-fluid-051220-043904>.
- Lellouche, J.-M., and Coauthors, 2018: Recent updates to the Copernicus Marine Service global ocean monitoring and forecasting real-time 1/12° high-resolution system. *Ocean Sci.*, **14**, 1093–1126, <https://doi.org/10.5194/os-14-1093-2018>.
- Lemarié, F., J. Kurian, A. F. Shchepetkin, M. J. Molemaker, F. Colas, and J. C. McWilliams, 2012: Are there inescapable issues prohibiting the use of terrain-following coordinates in climate models? *Ocean Model.*, **42**, 57–79, <https://doi.org/10.1016/j.ocemod.2011.11.007>.
- Mahadevan, A., A. Pascual, D. L. Rudnick, S. Ruiz, J. Tintoré, and E. D’Asaro, 2020: Coherent pathways for vertical transport from the surface ocean to interior. *Bull. Amer. Meteor. Soc.*, **101**, E1996–E2004, <https://doi.org/10.1175/BAMS-D-19-0305.1>.
- Marchesiello, P., L. Debreu, and X. Couvelard, 2009: Spurious diapycnal mixing in terrain-following coordinate models: The problem and a solution. *Ocean Model.*, **26**, 156–169, <https://doi.org/10.1016/j.ocemod.2008.09.004>.
- Mashayek, A., J. Gula, L. E. Baker, A. C. Naveira Garabato, L. Cimoli, J. J. Riley, and C. de Lavergne, 2024: On the role of seamounts in upwelling deep-ocean waters through turbulent mixing. *Proc. Natl. Acad. Sci. USA*, **121**, e2322163121, <https://doi.org/10.1073/pnas.2322163121>.
- Mason, E., J. Molemaker, A. F. Shchepetkin, F. Colas, J. C. McWilliams, and P. Sangrà, 2010: Procedures for offline grid nesting in regional ocean models. *Ocean Model.*, **35** (1–2), 1–15, <https://doi.org/10.1016/j.ocemod.2010.05.007>.
- , S. Ruiz, R. Bourdalle-Badie, G. Reffray, M. García-Sotillo, and A. Pascual, 2019: New insight into 3-D mesoscale eddy properties from CMEMS operational models in the western Mediterranean. *Ocean Sci.*, **15**, 1111–1131, <https://doi.org/10.5194/os-15-1111-2019>.
- McDougall, T. J., and R. Ferrari, 2017: Abyssal upwelling and downwelling driven by near-boundary mixing. *J. Phys. Oceanogr.*, **47**, 261–283, <https://doi.org/10.1175/JPO-D-16-0082.1>.
- Merryfield, W. J., and G. Holloway, 1999: Eddy fluxes and topography in stratified quasi-geostrophic models. *J. Fluid Mech.*, **380**, 59–80, <https://doi.org/10.1017/S0022112098003656>.
- Molemaker, M. J., J. C. McWilliams, and W. K. Dewar, 2015: Submesoscale instability and generation of mesoscale anticyclones near a separation of the California undercurrent. *J. Phys. Oceanogr.*, **45**, 613–629, <https://doi.org/10.1175/JPO-D-13-0225.1>.
- Munk, W. H., 1966: Abyssal recipes. *Deep-Sea Res. Oceanogr. Abstr.*, **13**, 707–730, [https://doi.org/10.1016/0011-7471\(66\)90602-4](https://doi.org/10.1016/0011-7471(66)90602-4).
- Naveira Garabato, A. C., K. L. Polzin, B. A. King, K. J. Heywood, and M. Visbeck, 2004: Widespread intense turbulent mixing in the Southern Ocean. *Science*, **303**, 210–213, <https://doi.org/10.1126/science.1090929>.
- , and Coauthors, 2019: Rapid mixing and exchange of deep-ocean waters in an abyssal boundary current. *Proc. Natl. Acad. Sci. USA*, **116**, 13 233–13 238, <https://doi.org/10.1073/pnas.1904087116>.
- Peterson, H. G., and J. Callies, 2022: Rapid spin up and spin down of flow along slopes. *J. Phys. Oceanogr.*, **52**, 579–596, <https://doi.org/10.1175/JPO-D-21-0173.1>.
- , and —, 2023: Coupling between abyssal boundary layers and the interior ocean in the absence of along-slope variations. *J. Phys. Oceanogr.*, **53**, 307–322, <https://doi.org/10.1175/JPO-D-22-0082.1>.
- Phillips, O. M., 1970: On flows induced by diffusion in a stably stratified fluid. *Deep-Sea Res. Oceanogr. Abstr.*, **17**, 435–443, [https://doi.org/10.1016/0011-7471\(70\)90058-6](https://doi.org/10.1016/0011-7471(70)90058-6).
- Rhines, P. B., and W. R. Holland, 1979: A theoretical discussion of eddy-driven mean flows. *Dyn. Atmos. Oceans*, **3**, 289–325, [https://doi.org/10.1016/0377-0265\(79\)90015-0](https://doi.org/10.1016/0377-0265(79)90015-0).
- Ruan, X., A. F. Thompson, and J. R. Taylor, 2019: The evolution and arrest of a turbulent stratified oceanic bottom boundary

- layer over a slope: Downslope regime. *J. Phys. Oceanogr.*, **49**, 469–487, <https://doi.org/10.1175/JPO-D-18-0079.1>.
- , —, and —, 2021: The evolution and arrest of a turbulent stratified oceanic bottom boundary layer over a slope: Upslope regime and PV dynamics. *J. Phys. Oceanogr.*, **51**, 1077–1089, <https://doi.org/10.1175/JPO-D-20-0168.1>.
- Salmon, R., G. Holloway, and M. C. Hendershott, 1976: The equilibrium statistical mechanics of simple quasi-geostrophic models. *J. Fluid Mech.*, **75**, 691–703, <https://doi.org/10.1017/S0022112076000463>.
- Sánchez-Garrido, J. C., and I. Nadal, 2022: The Alboran Sea circulation and its biological response: A review. *Front. Mar. Sci.*, **9**, 933390, <https://doi.org/10.3389/fmars.2022.933390>.
- Saunders, P. M., and B. A. King, 1995: Bottom currents derived from a shipborne ADCP on WOCE Cruise A11 in the South Atlantic. *J. Phys. Oceanogr.*, **25**, 329–347, [https://doi.org/10.1175/1520-0485\(1995\)025<0329:BCDFAS>2.0.CO;2](https://doi.org/10.1175/1520-0485(1995)025<0329:BCDFAS>2.0.CO;2).
- Shchepetkin, A. F., 2015: An adaptive, Courant-number-dependent implicit scheme for vertical advection in oceanic modeling. *Ocean Modell.*, **91**, 38–69, <https://doi.org/10.1016/j.ocemod.2015.03.006>.
- , and J. C. McWilliams, 2005: The Regional Oceanic Modeling System (ROMS): A split-explicit, free-surface, topography-following-coordinate oceanic model. *Ocean Modell.*, **9**, 347–404, <https://doi.org/10.1016/j.ocemod.2004.08.002>.
- , and —, 2009: Computational kernel algorithms for fine-scale, multi-process, longtime oceanic simulations. *Handbook of Numerical Analysis: Computational Methods for the Ocean and the Atmosphere*, R. M. Temam, and J. J. Tribbia, Eds., Vol. 14, Elsevier, 121–183.
- , and —, 2011: Accurate Boussinesq oceanic modeling with a practical, “Stiffened” Equation of State. *Ocean Modell.*, **38**, 41–70, <https://doi.org/10.1016/j.ocemod.2011.01.010>.
- Spingys, C. P., A. C. Naveira Garabato, S. Legg, K. L. Polzin, E. P. Abrahamsen, C. E. Buckingham, A. Forryan, and E. E. Frajka-Williams, 2021: Mixing and transformation in a deep western boundary current: A case study. *J. Phys. Oceanogr.*, **51**, 1205–1222, <https://doi.org/10.1175/JPO-D-20-0132.1>.
- Spurgin, J. M., and S. E. Allen, 2014: Flow dynamics around downwelling submarine canyons. *Ocean Sci.*, **10**, 799–819, <https://doi.org/10.5194/os-10-799-2014>.
- St. Laurent, L. C., J. M. Toole, and R. W. Schmitt, 2001: Buoyancy forcing by turbulence above rough topography in the abyssal Brazil Basin. *J. Phys. Oceanogr.*, **31**, 3476–3495, [https://doi.org/10.1175/1520-0485\(2001\)031<3476:BFBTAR>2.0.CO;2](https://doi.org/10.1175/1520-0485(2001)031<3476:BFBTAR>2.0.CO;2).
- Stewart, A. L., Y. Wang, A. Solodoch, R. Chen, and J. C. McWilliams, 2024: Formation of Eastern boundary undercurrents via mesoscale eddy rectification. *J. Phys. Oceanogr.*, **54**, 1765–1785, <https://doi.org/10.1175/JPO-D-23-0196.1>.
- Stommel, H., 1958: The abyssal circulation. *Deep-Sea Res.*, **5**, 80–82, [https://doi.org/10.1016/S0146-6291\(58\)80014-4](https://doi.org/10.1016/S0146-6291(58)80014-4).
- Thompson, L., and G. C. Johnson, 1996: Abyssal currents generated by diffusion and geothermal heating over rises. *Deep-Sea Res. I*, **43**, 193–211, [https://doi.org/10.1016/0967-0637\(96\)00095-7](https://doi.org/10.1016/0967-0637(96)00095-7).
- Tintore, J., P. E. La Violette, I. Blade, and A. Cruzado, 1988: A study of an intense density front in the Eastern Alboran Sea: The Almeria–Oran front. *J. Phys. Oceanogr.*, **18**, 1384–1397, [https://doi.org/10.1175/1520-0485\(1988\)018<1384:ASOAID>2.0.CO;2](https://doi.org/10.1175/1520-0485(1988)018<1384:ASOAID>2.0.CO;2).
- Vargas-Yáñez, M., F. Plaza, J. García-Lafuente, T. Sarhan, J. M. Vargas, and P. Vélez-Belchí, 2002: About the seasonal variability of the Alboran Sea circulation. *J. Mar. Syst.*, **35**, 229–248, [https://doi.org/10.1016/S0924-7963\(02\)00128-8](https://doi.org/10.1016/S0924-7963(02)00128-8).
- Venaille, A., 2012: Bottom-trapped currents as statistical equilibrium states above topographic anomalies. *J. Fluid Mech.*, **699**, 500–510, <https://doi.org/10.1017/jfm.2012.146>.
- Viúdez, Á., J. Tintoré, and R. L. Haney, 1996: Circulation in the Alboran Sea as determined by quasi-synoptic hydrographic observations. Part I: Three-dimensional structure of the two anticyclonic gyres. *J. Phys. Oceanogr.*, **26**, 684–705, [https://doi.org/10.1175/1520-0485\(1996\)026<0684:CITASA>2.0.CO;2](https://doi.org/10.1175/1520-0485(1996)026<0684:CITASA>2.0.CO;2).
- Waterhouse, A. F., and Coauthors, 2014: Global patterns of diapycnal mixing from measurements of the turbulent dissipation rate. *J. Phys. Oceanogr.*, **44**, 1854–1872, <https://doi.org/10.1175/JPO-D-13-0104.1>.
- Weijer, W., A. Barthel, M. Veneziani, and H. Steiner, 2020: The Zapiola Anticyclone: A Lagrangian study of its kinematics in an eddy-permitting ocean model. *Deep-Sea Res. I*, **164**, 103308, <https://doi.org/10.1016/j.dsr.2020.103308>.
- Wenegrat, J. O., and L. N. Thomas, 2020: Centrifugal and symmetric instability during Ekman adjustment of the bottom boundary layer. *J. Phys. Oceanogr.*, **50**, 1793–1812, <https://doi.org/10.1175/JPO-D-20-0027.1>.
- Wunsch, C., 1970: On oceanic boundary mixing. *Deep-Sea Res. Oceanogr. Abstr.*, **17**, 293–301, [https://doi.org/10.1016/0011-7471\(70\)90022-7](https://doi.org/10.1016/0011-7471(70)90022-7).
- Wynne-Cattanach, B. L., and Coauthors, 2024: Observations of diapycnal upwelling within a sloping submarine canyon. *Nature*, **630**, 884–890, <https://doi.org/10.1038/s41586-024-07411-2>.
- Xie, X., and Coauthors, 2022: Enhanced near-bottom circulation and mixing driven by the surface eddies over abyssal seamounts. *Prog. Oceanogr.*, **208**, 102896, <https://doi.org/10.1016/j.pocean.2022.102896>.